Title

Temporal Evolution of Volcanic Eruption, Fluvial Drainage Systems and Faulting on the Northwest Flank of Alba Patera as Revealed by Photogeological Mapping

Author

Chowdhury, Diya

Publication Date

2012

Peer reviewed|Thesis/dissertation

UNIVERSITY OF CALIFORNIA

Los Angeles

Temporal Evolution of Volcanic Eruption, Fluvial Drainage Systems and Faulting on the Northwest Flank of Alba Patera as Revealed by Photogeological Mapping

A thesis submitted in partial satisfaction of the requirements for the degree Master of Science in Geology

by

Diya Chowdhury

2013

ABSTRACT OF THE THESIS

Temporal Evolution of Volcanic Eruption, Fluvial Drainage Systems and Faulting on the Northwest Flank of Alba Patera as Revealed by Photogeological Mapping

by

Diya Chowdhury

Masters of Science in Geology

University of California, Los Angeles, 2013

Professor Gilles Peltzer, Chair

Although Alba Patera is the largest volcano in aerial extent in the solar system (~6.8 km high and >1000 km in radius), the geologic processes responsible for shaping its exceedingly low-angle flanks remain poorly constrained. These flanks are covered in lava flows, valleys and both radial and annular grabens. Previous attempts, limited by the resolution of the satellite images, assume that the annular grabens formed during the terminal stage of volcanic development whereas surface water flow occurred in the early stage of volcanic construction. In this study, we analyze high-resolution CTX satellite images in conjunction with digital topographic data from MOLA. Our work reveals complex cross cutting relationships between faults, drainage network development and lava flows on

the northwestern flank of Alba Patera. We observe a minimum of three generations of lava flows, three generations of drainage channels and three generations of faults. Mutual and successive cross-cutting relationships between drainage channels and faults indicate that the tectonic processes responsible for creating grabens on the volcano flank operated continuously and were coeval with drainage formation.

The lava flows are observed to be the oldest geomorphic features and the third generation of faults as the youngest geomorphic features in our mapped region. Crater counting indicates that the surface within the mapped region is Amazonian in age. An analysis of the crater densities reveals a decline in crater densities from the south to the north section of the mapped region. This could be attributed to resurfacing in the north due to sediments deposited by northward flowing drainage channels. Crater counting age estimates for the south section yield a result of ~ 1.74 Ga, +/- 0.12 Ga and ~ 1.35 Ga, +/- 0.26 Ga for the north section. Hence, the younger age estimates of the northern surface could help further constrain the age of the drainage channels and faults on the northwest flank of Alba Patera.

The thesis of Diya Chowdhury is approved.

An Yin

David Paige

Gilles Peltzer, Committee Chair

University of California, Los Angeles

2013

TABLE OF CONTENTS

ACKNOWLEDGEMENTS

I would first like to thank my advisor, Gilles Peltzer for providing me with the opportunity to work on this project. His tireless mind and devotion to science and education has been crucial to developing this thesis. I thank An Yin for his expert guidance in shaping this project. His enthusiasm for exploration has been a great source of inspiration for my research. I thank David Paige for his valuable input and encouragement towards this poject.

I owe many thanks to my classmates and colleagues at UCLA, specifically Jessica Watkins and Jennifer Scully. Scientific discussions aided by their brilliant minds helped stimulate many ideas during the process of writing this thesis. Credit must also be given to all the scientists working to make high-resolution data such as MOLA, CTX and softwares such as Isis freely available to us. I thank Trent Hare of the U. S. Geologic Survey and Antoine Lucas for their help with processing data and troubleshooting software. Last but not the least, I thank my family for their infallible support in my every endeavor. This work would not have been possible without them.

INTRODUCTION

1.1 THE PLANET MARS

Mars is about half the size of the Earth, with a mean radius of 3389 km. It is at a distance of 55.7 – 401.3 x 10^6 km from the Earth, a vast range due to the difference in ellipticity of their orbits around the Sun. The orbital eccentricity of Mars ranges between 0 and 0.12, affecting the duration and intensity of seasons. The planet receives 45% more sunlight at perihelion than at aphelion (Carr, 2006). Since the perihelion occurs at the end of the spring in the southern Hemisphere, the southern springs and summers are thus hotter and shorter than those in the northern hemisphere (e.g., Smith et al., 2004; Murchie et al. 2007). The current atmosphere of Mars consists mostly of CO_2 with the average surface pressure ranging from 6.9 to 9 mbar (Hess et al., 1980). Unlike the Earth's atmosphere, Mars lacks an ozone layer and is extremely rich in dust (e.g., Zureck et al., 1992; Clancy et al., 2000; Smith, 2004). Up to elevations of approximately 100 km, the Martian temperature is controlled by factors such as heat exchange with the surface, radiative emission and absorption of heat by CO_2, which result in a decrease in temperature with altitude (e.g., Zureck et al., 1992; Clancy et al., 1990; Clancy et al., 2000; Smith, 2004). Above 110 km, temperatures begin to rise with altitude due to the absorption of extreme UV radiation, similar to Earth (e.g., Zureck et al., 1992; Clancy et al., 1990; Clancy et al., 2000; Smith, 2004). Since the Martian atmosphere is dry and thin, it absorbs very little of the Sun's heat, resulting in a wide range of surface temperatures for

most of the year. A typical day lasts for 24 hr 39.6 min. Surface temperatures depend on latitude, season, albedo, thermal inertia, and topography of the surface (Carr, 2006).

It is crucial that one keeps these characteristics in mind when studying the surface processes on Mars, especially when using remote-sensing data. The evolution of landforms is vastly dependent on climate conditions and conversely, geomorphic features can serve as good indicators of past climate conditions.

1.2 THE SURFACE OF MARS

It is widely accepted that Mars is differentiated into a core, mantle and crust (Dehant et al., 2003; Mezger et al., 2012). The thickness of each layer is poorly defined due to the lack of seismic data (Stevenson, 2001). However, NASA recently proposed a Discovery Program mission called InSight that will involve placing a geophysical lander on Mars to study its deep interior. Present day Mars has no global magnetic dipole (Stevenson, 2001), suggesting that the dynamo has ceased to operate (e.g., Acuna et al., 1999; Stevenson, 2001; Dehant et al., 2003). However, there is evidence of remnant magnetism in crustal rocks indicating a more active core earlier in the planet's history (e.g., Acuna et al, 1999; Stevenson, 2001; Lillis et al., 2009).

Mars' crust is basaltic in composition, with a few siliceous rocks (McSween et al., 2009). Due to lower gravity, lower atmospheric pressure and different structure of the crust, basaltic flows behave differently on Mars than on Earth (e.g., Wilson and Head, 1994, Zuber et al. 2000; Werner, 2009). Baratoux et al. (2009)

compare effusion rates on Earth and Mars based on the volume of eruptions of the Central Elysium Planitia on Mars and the Hawaiian-Emperor chain on Earth. They conclude that the average eruption rate on Earth is two orders of magnitude greater than that on Mars. Thermal Emission Spectrometer (THEMIS) data of the crust below latitudes of 30° indicates a basaltic spectrum, transitioning to a more basaltic andesite composition above latitudes of 30° (Wyatt et al., 2004). The study attributes this observation to preferential weathering due to the presence of stable ice at higher latitudes.

The presence of water ice on Mars was long debated (Leighton & Murray, 1966; Sharp et al., 1971; Carr & Schaber, 1977; Squyres & Carr, 1986, Paige, 1992) until data acquired by the Gamma Ray Spectrometer (GRS) on board the Mars Odyssey spacecraft provided evidence for it (Boynton et al., 2002; Feldman et al., 2002; Mitrofanov et al., 2002). This discovery is of special interest due to the biological implications. Although geomorphic indicators provide strong evidence of its presence in the past (Sharp et al., 1971; Carr & Schaber, 1977; Squyres &Carr, 1986), present day conditions would make liquid water unstable on the surface of Mars. Carr (2006) suggests that surface water could indeed have existed on the surface, but under different weather conditions. Many valley networks have been observed on Mars, mostly in the cratered uplands. Martian valleys are seen to be long and narrow, with steep slopes and cross sectional shapes ranging from V-shaped in the upper reaches to U-shaped in the lower reaches (Carr, 2006; Ivanov & Head, 2006).

The Martian surface has been divided into three stratigraphic sections of age

based on crater counting (Tanaka, 1986) (Fig. 1). The first system dates back to the late heavy bombardment, during which time the rate of impact on Mars was the highest in the history of the planet, and is known as the Noachian age. This period is estimated to have dated from ~4.1 Gy through ~3.7Gy (Hartmann and Neukum, 2001), preceding the Hesperian age. The Hesperian age shows a marked decline in impacts of the surface, dating from ~3.7Gy to ~2.9-3.1Gy (Hartmann and Neukum, 2001). All the features that formed from then till the present day are said to be of Amazonian age.

The topography of Mars shows a distinct difference in elevations between the northern and southern hemispheres (Fig. 2). This global dichotomy is apparent in the positive topography of the southern hemisphere and negative topography of the northern hemisphere with respect to the spherical reference surface of Mars (Carr, 2006). Apart from this dichotomy, Mars' topography also boasts some of the largest volcanoes and valley systems in the Solar System (Fig. 2)

1.3 ALBA PATERA

Alba Patera is the largest volcano in the solar system in aerial extent (Figs. 2, 3), centered at 40°N, 109°W (Fig. 2) (e.g., Mouginis-Mark et al., 1988). It is also one of the youngest volcanoes on Mars. It is classified as a shield volcano based on its gentle slope and expansive basalt flows. Extensive flows indicate a low viscosity flow material, estimated at ~ $4x10^6$ Pa (Hiesinger et al., 2007), allowing them to spread over a larger extent. Lava flows extend from 26°N in the south to 61°N to the north (e.g., Carr, 2006; Ivanov & Head, 2006). The maximum age of

the flows are determined to be ~3.5 Ga (Neukum & Hiller, 1981; Wener, 2005). At least 4 episodes of activity are observed on the western flank of Alba Patera dated at 3.4Ga, 2Ga, 800 Ma and 250 Ma (Werner, 2005). Crater counting ages on other parts of the volcano fall between 1.1 Ga to 3 Ga (Werner, 2005).

Scott & Tanaka (1986) classify the flows on Alba Patera into 3 units based on age (Fig 1). The lower member (Hal) is Hesperian in age, corresponding to the flows outside the main construct. However, unit Hal is suggested to have been derived from Uranius Patera volcanism, rather than Alba Patera (Carr, 2006; Yin, 2012). The middle member (Aam) is early Amazonian in age and corresponds to the main volcanic construct. The upper member (Aum) is also upper Amazonian in age and corresponds to the summit of the volcano. These flows can be further divided into two types: sheet flows and tube flows. Sheet flows are broad and flat-topped whereas tube flows are long and ridge-like. The tube flows extend over hundreds of kilometers on the western flank, the edges of which are usually gullied.

The diameter of Alba Patera ranges from 2000 km measured in the North-South direction and 3000 km in the East-West direction. The average slope of the volcano is 0.5°, with the summit rising to elevations of 6800 m (e.g., Carr, 2006; Ivanov & Head, 2006). Topographic profiles show the presence of two lobes on the eastern and western side of the central edifice, with the summit sloping distinctly to the east (e.g., McGovern et al., 2001; Ivanov & Head, 2006). Ivanov & Head (2006) suggest that summit tilting took place at a later stage of volcanic construct, based on the symmetric pattern of lava flow around the summit. Alba

Patera is located at the northernmost boundary of the Tharsis rise. Tharsis is an 11,000 m high and 8000 km wide volcanic dome at the equator of Mars. The proximity of Alba Patera to Tharsis results in a delicate balance of regional and local stresses affecting the structure of Alba Patera, as discussed below (e.g., Ivanov & Head, 2006; Yin, 2012).

One of the most striking features on Alba Patera is the colossal fractures (Fig. 3). Tanaka (1990) attributes faulting in this region to a combination of Alba Patera magmatism, Tharsis-centered tectonism and the presence of the dichotomy boundary. He also suggests that these faults evolved over a long period right from the Noachian to the late Amazonian period. Based on their orientation, faults on Alba Patera can be divided into two distinct groups. The first set forms circumferential grabens (Fig. 3) around the caldera and is suggested to be the result of subsidence in the latter stages of volcanic construction (e.g., McGovern et al., 2001; Cailleau et al., 2003; Ivanov & Head, 2006). The second set is a combination of Ceraunius Fossae (Fig. 3A) to the south and the Noachian NE-SW trending faults northeast of the volcano (Fig. 3B) (Tanaka, 1990). Ceraunius Fossae is an area heavily transected by north-trending faults initiated in the Late Noachian (~ 4.20 Ga – 3.50 Ga) to Late Hesperian (~ 3.70 Ga to 1.80 Ga) epochs (Tanaka, 1990). The formation of these radial grabens south of Alba Patera, have been attributed to regional extension due to Tharsis activity (Tanaka et al., 1991), deflecting around the volcanic center of the volcano to the north (Raitala, 1988).

Extension on Mars is also suggested to form pit crater chains. Pit crater chains

are linearly aligned circular to elliptical depressions. The individual depressions lack ejecta or elevated rims that are usually associated with impact craters (Wyrick et al., 2004). Very little is understood about them but Wyrick et al. (2004) and Ferrill et al. (2004) suggest that their formation is the result of collapse of material into a subsurface cavity. Wyrick et al. highlight dilatational normal faulting and sub-vertical fissuring as the main cause of the formation of pit crater chains. However, dike emplacement is also suggested to create chains of pit craters on Alba Patera (Scott and Wilson, 2002). According to their study, the collapse could be the result of degassing of a stalled dike.

Fractures and pit crater chains can easily be confused with the valley networks also observed on the flanks of Alba Patera. They are abundant and thought to be fluvial in origin (Gulick & Baker, 1990), representing branched systems of valleys that resemble fluvial drainages on Earth. They will henceforth be referred to as drainage channels. Based on topographic profiles, the drainage valleys are suggested to be younger than the lava flows on the northern flank (Ivanov & Head, 2006). However, lava sheet flows can be seen to embay small valley networks on the western flank of Alba Patera (Ivanov & Head, 2006). Furthermore, drainages are observed to form preferentially on the northern flank (Ivanov & Head, 2006). Ivanov & Head (2006) suggest the presence of an ice-rich dust layer, emplaced prior to valley network formation. It follows that this region is affected by geothermal activity, resulting in the formation of drainage channels. Hence, they explain the preferential formation of drainage channels on the northern flank rather than the southern, based on interpretations of water ice

being transported to lower latitudes from Polar regions during periods of high obliquity for Mars (Richardson & Wilson, 2002; Haberle et al., 2003).

Recently acquired higher resolution THEMIS daytime IR and MOLA data reveal more channels per unit area than previously observed on Mars, suggesting a large source of water for these drainages (Hynek et al., 2010). They point out that the northwest flank of Alba Patera contains the densest set of young valleys on Mars. The study compares the decay of drainage density through time on various volcanoes on Mars. Due to the anomalous values of drainage channels Alba Patera in comparison to channels on other volcanoes on Mars, they infer that the drainage systems on Alba Patera are precipitation fed (Fig. 5). These inferences are in agreement with Baker et al. (1991) and Baker (2001) who suggested that the valleys on Alba Patera in specific formed by precipitation during a time of warmer climate in Mars' past.

Mouginis-Mark et al. (1988) propose a 5-stage model for the evolution of Alba Patera (Fig. 4). Activity begins with an explosive eruption of an ash layer, followed by summit lava flow emplacement. The presence of a pyroclastic layer is in agreement with Wilson & Head (1994). Next, melt-water is released from the volatile rich ash layer forming drainage channels. Activity ends with summit collapse and the formation of concentric faulting around the caldera. Ivanov & Head (2006) also agree that there is a change in the style of eruptive volcanism with time on Alba Patera. Yin (2012) suggests that this mixed mode of eruption demonstrated by Alba patera, from explosive to effusive, indicates a temporal evolution of the volcanic system, possibly to do with the amount of volatiles in the

magma chamber.

1.4 AIMS OF THIS STUDY

This study attempts to understand both the tectonic and fluvial systems on Alba Patera. We analyze the northwest flank of Alba Patera via photogeological mapping, closely observing cross-cutting relations between 3 main morphological features; faults, drainage channels and flow margins. This helps better understand the chronology of events that took place in this region. Our results are combined with crater counting data, adding further constraints on the ages of these events. The significance of this work is in distinguishing a sequence of discrete events that affected this region. Comparing our results to previous work will help reconstruct the history of Alba Patera. Furthermore, such an understanding would help us attribute specific events to specific processes that were active on Alba Patera, and in effect, the surface of Mars. To simplify the tectonic context of our analysis, we choose a study area that includes only the circumferential faults on the northwest flank of Alba Patera. Our results suggest that the lava flows were the oldest event and that drainage formation was coeval with circumferential faulting on the northwest flank of Alba Patera.

2 DATA AND METHODS

2.1 MARS IMAGERY AND PHOTOGRAPHY DATA

The exploration of Mars through remote sensing began with the Mariner missions. The first successful mission was the Mariner 4 spacecraft, launched by NASA in November of 1964. It was a fly by mission, providing us with our first images of Mars (Leighton et al., 1965). However, it was the Viking missions, launched in August (Viking 1) and September (Viking 2) of 1975 that were truly instrumental in encouraging the study of the geology on Mars (Cutts et al., 1976; Carr, 1979 etc.). The orbiters imaged the entire surface of Mars at a resolution of 150 to 300m, and selected areas at 8m.

As technology progressed, so did the complexity of these projects providing us with higher resolution data to help understand Mars better. The first instrument to collect topography data of Mars was the Mars Orbiter Laser Altimeter (MOLA) on the Mars Global Surveryor (MGS) spacecraft. This mission was launched in November of 1996 by NASA. The data collected have a resolution of 463.1 m/pixel. The MGS also carried on board the Mars Orbiter Camera (MOC), with the narrow angle grayscale camera providing us with images of Mars at a resolution of 1.5-12 m/pixel, and the red and blue wide angle cameras providing context images (240 m/pixel) and daily global images (7.5 km/pixel).

In February of 2003, the European Space Agency (ESA) launched the Mars Express spacecraft providing us with even higher resolution topography data of Mars. This data set was obtained by the High-Resolution Stereo Camera (HRSC)

that provides us with both optical images (2m/pixel) and stereo images (10m/pixel).

Finally, in August of 2005, NASA launched the Mars Reconnaissance Orbiter (MRO) providing us with the highest resolution images of Mars to date. On board is the High Resolution Science Experiment camera (HiRISE) providing us with images in the visible region of the spectrum with resolutions varying from 0.3-0.6m/pixel. Also on board the MRO are the Compact Reconnaissance Imaging Spectrometer for Mars (CRISM) and the Context camera (CTX). CRISM collects spectral data in the visible and infrared wavelengths with resolutions of up to 18m/pixel, and CTX, as the name suggests, collects context images with resolutions up to 6m/pixel.

In this study CTX data is used to create a mosaic of our study region. This mosaic is complemented by HRSC optical images of the same region. We also use MOLA and HRSC topography data to better understand the structure of the flanks of Alba Patera.

2.2 DATA PROCESSING

All CTX data is managed by the School of Earth and Space Exploration at Arizona State University. The CTX data was processed using Isis, an image processing software package developed by the United States Geological Survey (USGS) (Torson & Becker, 1997). Isis is used to correct and calibrate image data collected by current and past NASA planetary missions. Raw CTX data is used which is first radiometrically corrected in Isis. Next, the even/odd detector striping

is removed, which would otherwise cause vertical striping in the image. This is fixed by averaging over the even and odd columns and dividing the difference by two, applying these offsets to both columns (isis.astrogeology.usgs.gov). For the purpose of this study, we use Isis to combine 5 CTX images. Since CTX images are slanted, the mosaic extends from 113°20’20’’W to 111°50’10’’W in the north and 112°50’70’’W to 111°20’70’’ in the south (Fig. 8). This mosaic is projected in a sinusoidal projection with the brightness and contrast of each image tone matched to all the other images in the mosaic.

Next, the pixel values of the mosaic are stretched linearly, between values of 0 to 255 after which the mosaic is imported into ArcGIS Desktop v. 10 for mapping. ArcGIS is a software developed by the Environmental Systems Research Institute (ESRI) which can be used to perform geo-processing functions such as spatial analysis, data management, mapping, geo-coding etc. Once opened in ArcGIS, a geo-database is created with our mapped units stored as vectors. These vectors can then be easily manipulated to map over our basemap. Finally, these mapped units are laid over HRSC topography data in ArcView to allow us to analyze the results in 3D.

As the availability of HRSC topography data in our mapped region is limited, lower resolution MOLA data is also studied. The MOLA data is imported into ENVI, a software developed by Exelis Visual Information Solutions (Exelis VIS), to process and analyze geospatial imagery. Once imported in to ENVI, vertical profiles are studied to better understand the volcanic construct of Alba Patera.

In the past, similarities between the geologic features seen on Earth and Mars

have all been revealed by remote sensing (Carr, 1977). With high-resolution data now readily available for Mars, superficial features such as fluvial valleys, landslides and sand dunes can be identified. However, it is important to mention that although remote sensing techniques have been pivotal in understanding the surface of Mars, our sole dependence on it has limited us in revealing other characteristics such as the ages of features etc. At present, methods such crater counting and cross-cutting relations are used to date features on Mars (Carr, 2006).

2.3 MAPPING CRITERIA

This section discusses the various criteria used to distinguish lava flows, faults, drainage channels and craters in our region of interest. Criteria are adopted to best serve the purpose of understanding the chronology of events via cross-cutting relations between features. Faults are observed to cross-cut drainages and vice versa. Using the criteria mentioned below, faults and drainages are divided into various generations based on which feature cross-cuts into the other.

2.3.1 LAVA FLOWS

Flow margins are degraded and difficult to define in our study region (Fig. 7). Although flow margins are identifiable towards the North, they cannot be traced back to the source point in the south section of the mapped region. This is due to the combination of the image resolution as well as stretching the pixel values in order to read the data in ArcGIS. For this reason, lava flows are mapped only on

local maps (Figs. 8h, i, j, l, o, p). In these local maps, they are mapped based on the superposition of flow edges. As the source points of the lava flows are unknown, each flow margin is regarded to represent a separate flow (Figs. 8h, i, j, l, o, p).

2.3.2 FAULTS

Faults on Alba Patera can easily be confused with other morphological features, such as pit crater chains and drainage channels. Keeping this in mind, below is a list of the mapping criteria devised to identify faults in our study area.

1. Fractures along which scarps can be distinguished are characterized as faults.
2. Fragments of faults that are in contact with each other are assigned the same generation (Fig. 8a).
3. Faults cross-cut by drainage channels are interpreted as belonging to an older generation than said drainage channel (Fig. 8e).
4. Faults which cross-cuts drainage channels are interpreted as belonging to a younger generation than said drainage channel (Fig. 8g).
5. Faults that are neither connected to adjacent faults nor cross-cut by any other feature are designated as unknown faults (Fig. 8b).

2.3.3 DRAINAGE CHANNELS

Drainage channels in our mapped region are identified based on characteristics of drainages on Earth (Fig. 6). Below are the mapping criteria adopted to map drainage channels in our study area.

1. Channels are characterized by narrow sinuous valleys that generally increase in width down slope and divide into smaller branches up slope. This is similar to the classification adopted by Carr (1995).
2. Drainage channels cross-cut by a faults are interpreted as belonging to an older generation than said fault (Fig. 8g).
3. Drainage channels which cross-cuts faults are interpreted as belonging to a younger generation than said fault (Fig. 8e).
4. When two or more channels of different generations meet, the confluent channel is assigned the same generation as that of the younger channel (Fig. 8k). This implies that the confluent channel was active right from the older channel's age through the younger channel's age. Hence we assume the youngest possible chronology for the confluent drainage channel.
5. If sediment deposition is observed at the point of confluence of a tributary to a main drainage channel, the tributary is considered to be older than the main channel (Fig. 8c).
6. Drainage channels which are disconnected from adjacent channels are interpreted as 1st generation, unless cross cutting relations indicate otherwise (Fig. 8d).

2.4 CRATER COUNTING

Craters are the result of high velocity impacts between planetary bodies and comets or asteroids. Although rare on Earth because of constant resurfacing, they are commonly observed on other planetary bodies. Based on lunar records,

the rate of collision has been inferred to be stable over the past 3.5 Gyr. However, the impact rate used to be as much as 500 times higher 4 Gyr ago (Nuekmann et al., 2001).

The observations make craters a helpful tool in gauging the age of planetary surfaces. A statistical analysis of crater size-frequency distributions (CSFDs) per unit area calibrated by radiometrically determined ages of rock samples on the moon were used by Neukum & Wise (1976) to establish a Moon-wide relative and absolute chronology. These results have now been calibrated for different terrestrial planets and satellites (Neukum et al., 2001a; Ivanov, 2001; Hartmann & Neukum, 2001). All of these studies now allow us to determine the ages of planetary surfaces from satellite images. Crater counting has been used to distinguish the three major time periods on Mars, ie – Noachian, Hesperian and Amazonian. Although it is a widely used method, it must be noted that as craters are a surface process, they are prone to weathering and alteration. This implies that the method of crater counting provides us only with the younger age limit for all surfaces.

The CFSDs per unit area on the lava flows are analyzed within the study area (Fig. 9). The cratering chronology function as described by Hartmann &Neukum (2001) is applied and the impact crater production function as described by Ivanov (2001). All measurements and calculations are done via CraterTools; a map projection-independent crater size-frequency determinate toolbar for ArcGIS designed by Kneissl et al. (2011). Craters are mapped by manually selecting opposite ends of the diameter of a crater, around which CraterTools constructs a

circle to fit. Hence all craters are assumed to be circular. Limited by the resolution of our base map, all craters above a diameter of 100 m are mapped. Craters are included regardless of the level of degradation. Due to the extensive characteristic of the flows on Alba Patera, it is assumed that any craters resulting from older impacts would be obliterated by the lava flows.

Results from CraterTools are then imported into Craterstats2 (Neukum, 1983; Michael & Neukum, 2010; Michael et al., 2011), a software that can plot isochrons for the best fit for age determination. Errors in observations are introduced primarily due to map projection of base maps and the assumption that all craters are circular. Elliptical crater rims present the problem in that they have two possible diameters, ie – the major axis and the minor axis. As a result, this would affect the crater-size frequency distribution of a given surface, reflected in the age estimates. Error estimates are discussed in further detail in Keissl et al. (2011).

3 RESULTS

Although we see multiple flow margins in our mapped region, the inability to trace each individual flow to the source leaves us with inconclusive results as to the absolute number of lava flows. However, flow margins are less degraded and easier to distinguish farther away from the source, towards the North of the map. We observe a maximum of 3 distinct superposed flow margins in any one local map (Fig. 8i). This implies a minimum of 3 generations of lava flows in this region, with the possibility of more.

Circumferential faults expose massive scarps, forming grabens all around the summit, indicating a radial extension source (Fig. 7). In the study area, all faults have the same general SW-NE orientation. The faults differ vastly in length as well as the size of the scarp exposed. Since no cross-cutting of faults with lava flows or drainage channels are observed closer to the summit of the volcano, the top most faults are assumed to be of an unknown age.

In areas farther from the summit, cross-cutting relations between drainages and faults indicate a minimum of 3 generations of faults (Figs. 8a-r) that either cross-cut or are incised by drainage channels, based on the generation. No drainages are observed to cross-cut the 3rd generation of faults within the study area. Faults are observed to cut the lava flows, whereas no flows are observed to cover faults (Figs. 8h, i, j, l, o, p).

Drainage patterns observed in the study area are dendtritic (Fig. 7), resembling a tree-like branching system of tributaries converging in the downslope direction.

Similar to Hynek et al. (2010), a much higher density of drainage networks are observed in our study region compared to regions studied by Carr (1977) and Carr (1995). This is entirely due to the availability of higher resolution data today. Based on cross cutting relations and the mapping criteria mentioned above, 3 generations of drainage channels are observed (Figs. 7, 8l). All drainage channels are observed to incise into lava flows, but no laval flows are observed to cover drainages. This indicates that both the faults and drainages post-date the flows in our study region (Figs. 8h, i, j, l, o, p).

3.1 DESCRIPTION OF CROSS-CUTTING OBSERVATIONS

A close analysis of image data within our study region reveals a complex cross cutting geometry between faults and drainage channels, both of which cut into lava flows. Examples are discussed in further detail below.

1. Fig. 8e illustrates drainage channels cross-cutting a SE dipping fault. As the fault is a 1st generation fault, the drainage channels are interpreted as being younger, i.e. – 2nd generation drainage channels.
2. Following the 2nd generation drainage channels southward (Fig. 8), they are cross-cut by younger faults; ie – 2nd generation faults (Figs. 8f, g).
3. Figs. 8m and 8n clearly illustrate large 2nd generation drainage channels cutting into older 1st generation faults. Smaller and older 1nd generation drainage channels can be seen to join a younger 2nd generation channel in Fig. 8m. The 1st generation channels are cut off from the younger drainage

channel in the Fig. 8m.

4. Fig. 8h illustrates large drainage channels cross cutting older faults. The faults are 1st generation, implying that the drainage channels are 2nd generation. The edges of 2 separate lava flows are also be observed in the SW corner of Fig. 8h.
5. Following the drainage channels from Fig. 8h upstream to Fig 8l, 2 distinct lava flow margins are distinguished. All 3 generations are observed, with younger 2nd generation drainage channels cross-cutting 1st generation faults towards the east.
6. Following the above-mentioned 1st generation fault further east to Fig. 8j, more 2nd generation drainage channels are observed to cross cut the faults.
7. Further upstream (Fig. 8), these first generation faults are observed to be cross cut by younger 3rd generation drainage channels (Figs. 8o, k). These 3rd generation drainage channels are cross cut by even younger 3rd generation faults as observed in the SE corner of Fig. 8k. 2 distinct lava flows are also observed in Fig. 8o.
8. Farther to the east, Fig. 8i clearly illustrates the complex geometry in our mapped region. 3 superposed flow margins are observed with 1st and 2nd generation drainage channels cross cut by 1st and 2nd generation faults respectively. It is important to note that although flow edges appear to belong to the same lava flow, based on our mapping critera, unless the flow margin can be traced all the way, separate flow edges are interpreted to refer to separate flows.

9. Younger drainage channels are observed to flow into a graben and cutting into the faults in figure 8q. All features are superposed by impact ejecta in the SW corner of Fig. 8q.
10. Further north (Fig. 8), we see similar cross cutting between drainage channels and 1st generation faults (Fig. 8r). We also observe a small offset of an older 1st generation drainage channel by a younger 1st generation fault in the SE corner of Fig. 8r.

As illustrated above, 3 distinct generations of faults and 3 generations of drainage channels are observed in our study region, cross cutting each other at various instances (Figs. 8a-r). This indicates that drainage formation was coveal with faulting over Alba Patera.

3.2 DESCRIPTION OF CRATER-COUNTING OBSERVATIONS

A total of 1091 craters were mapped by this study, with diameters ranging from ~100 m to ~13 km. The craters are mapped on the lava flows, implying that our crater counting results refer to the age of the lava flows. By applying a crater production function for Mars as described by Ivanov (2001) and a crater chronology function for Mars as described by Hartmann & Neukum (2001), a cumulative fit provides us with ages between ~ 2.89 Ga, +0.32/-0.55 Ga to ~ 701 Ma, +/- 35 Ma for the entire mapped region (Fig. 9). This estimate indicates a surface which is Amazonian in age.

Close observation of the density of craters reveals a sharp decline in the density

of impact craters from the south to the north of the mapped region (Fig. 9). This could be the result of resurfacing in the north. Mapping indicates all drainage channels flowing northwards, suggesting the deposition of sediments in the north. Crater counting of the two sections separately reveals ages between ~ 3.24 Ga, +0.17/-0.60 Ga to ~ 885 Ma, +46/-47 Ma for the south section (Fig. 10) and ~ 2.49 Ga, +0.65/-0.82 Ga to ~ 678 Ma, +/- 100 Ma for the north section (Fig. 11). Although all of these results refer to the Amazonian age, the upper and lower limits for the north section are younger than those for the south section. This may suggest that the surface to the north is younger than that to the south of the mapped region.

4 DISCUSSION

Most of our inferences about the surface of Mars are based on our knowledge of the geomorphology on Earth. However, it is important to remember that the processes that form these landforms on Earth and Mars may not always be the same due to the difference in gravity, atmosphere, climate conditions etc. as mentioned above.

Lava flows in our study area are observed to be older than both faults and drainage channels based on the lack of any discernable cross cutting or superposition of flow margins over other features. This is contradictory to observations made by Ivanov & Head (2006) on the western slope of Alba Patera, where they distinguish sheet flows superposing drainage networks. A minimum of 3 generations of lava flows are observed in local maps of our study region, a possible indicator of multiple periods of eruption on Alba Patera, in agreement with Ivanov & Head (2006), Werner (2009) and Yin (2012).

Although in the case of volcanoes, drainage channels are easily confused with lava channels (Gulick and Baker, 1990), drainage channels on Alba Patera tend to originate from a single source, branching upstream. These characteristics are similar to fluvial valleys on Earth, indicating a similar source on Mars (Fig. 6) (e.g., Carr, 2006; Ivanov & Head 2006). In-depth mapping reveals a minimum of 3 generations of drainage channels and 3 generations of faults cross cutting each other in various examples (Fig. 8a-r). This indicates that drainage formation was coeval with faulting in the region.

These results contradict the discrete 5-stage model proposed by Mouginis-Mark et al. (1988). It also follows that the source for these drainage channels was active right through the faulting event(s). Most studies conclude that these young drainage channels on Alba Patera are the result of hydrothermal activity or groundwater sapping. The latter interpretation is based on the presence of alcove-like heads (Pieri, 1980; Carr & Clow, 1981; Carr, 1955 and Carr, 1996). However, based on recent revelations of the presence of a much higher density of drainage channels than previously thought, Hynek et al. (2010) suggest the presence of an alternative source.

An analysis of craters in the mapped region shows a distinct decrease in the density of craters in the north section compared to the south section (Figs. 9, 10, 11). Mapping indicates all drainage channels flowing northward. Hence the above-mentioned decline in crater density could be the result of resurfacing, brought about by the deposition of sediments by drainage channels. This is in agreement with Ivanov & Head (2006) who suggest that these easily erodable sediments on the northern flank of Alba Patera could be the pyroclastic deposits from previous volcanic eruptions. Fig. 12 shows a profile of the topography taken along the study region from the flank to the possible depositional area. Bases on interpretations of depositional environments on Earth, the part of the profile that concaves downward could be interpreted as the incised region of the slope. Conversely, the part of the profile that concaves upward could be interpreted as the depositional region of the slope. However, it is important to note that resurfacing could also be the result of other processes such as wind deposition.

Crater counting of the north and south sections separately reveals an age of approximately 1.35 Ga, +/- 0.26 Ga (Fig. 11) for the northern surface and an age of approximately 1.74 Ga, +/- 0.17 Ga (Fig. 10) for the southern surface. Both results imply an Amazonian age. Although these ages do not fall into one of the 4 discrete ages of eruption identified by Werner (2005) for the western flank of Alba Patera (ref. section 1.3), they are in general agreement with his ages. These results indicate a younger age for the north section than the south. This is in agreement with the possibility of resurfacing in the north mentioned above. Further, if resurfacing is indeed due to the deposition of sediments by drainage channels, the age of the northern surface could give us an indication of the age of the drainage channels in this region as well as the faults, due to their coeval relationship. Whereas age estimates for the south section could correspond to the age of the lava flows.

CONCLUSION

This study reveals drainage formation coeval with circumferential faulting in the northwest quadrant of Alba Patera. This would imply that the source of the drainage was active at the same time as faulting. Flows are interpreted to be older than both drainage channels and faults in the region. This is contradictory to observations made by Ivanov & Head (2006) on the western flank of Alba Patera, where lava sheet flows distinctly cover drainage channels.

Crater counting results for the entire mapped region indicates an age of approximately 1.46 Ga, +/- 0.11 Ga (Fig. 9) ie – Amazonian age. It then follows that both the drainage channels and the faults in this region would be younger than the above-mentioned age. However a closer analysis of the density of impact craters in the mapping area reveals a sharp decrease in crater densities from the north section to the south section. This could be the result of resurfacing due sediment deposition by north flowing drainage channels. Hence, the age of the northern surface could be an indication of the period during which the drainage channels were active, further constraining the age of the drainage channels in this region. Additionally, as the faults are coeval with the drainage channels, the age of the northern surface would also help constrain the age of the faults. Crater counting reveals ages of approximately 1.35 Ga, +/- 0.35 Ga for the northern surface and an age of approximately 1.74 Ga, +/- 0.17 Ga for the southern surface.

Future work includes better constraints on the ages of geomorphic features in

this region. CRISM data could also be included in the study, allowing us to distinguish between features based on compositional characteristics. Further, a larger area, connecting the western and northern sections of Alba Patera, could be studied for cross-cutting relations. This would help understand the change in flow activity from the west, where flows are seen to cover drainage channels (Ivanov & Head, 2006) to our study region in the northwest, where lava flows do not cover any feature. Finally, it would also be interesting to further analyze the margin between the north and south sections of our mapped region to look for geomorphic indicators such as deltas to better understand the nature of deposition in this area.

FIGURE CAPTIONS

Figure 1 (Ivanov & Head, 2006) Geologic map of the Tharsis Rise region superposed on a MOLA shaded relief map. Figure modified from Scott & Tanaka (1986). Refer to section 1.3 for description.

Figure 2 Topography of Mars by MOLA data (NASA). Box indicates the extent of Figure 3.

Figure 3 Shaded topography of Alba Patera region on Mars. Figure compiled with MOLA data processed in ArcGIS to produce a shaded hill effect. Highlighted area in red indicates study area and the extent of Figures 7 and 8. Box A – Ceraunius Fossae, Box B – Noachian NE_SW trending faults.

Figure 4 (Mouginis-Mark et al., 1988) 5-stage model of the evolution of Alba Patera. Refer to section 1.3 for description.

Figure 5 (Hynek et al., 2010) Normalized drainage density on all dissected volcanoes versus their surface age determined by crater counting. The black line represents the authors' interpretation of drainage density over time. Alba Patera illustrates distinct anomalous values, inferred by the authors to indicate a precipitation-fed drainage system.

Figure 6 (NASA/GSFC/METI/Japan Space Systems and U.S./Japan ASTER Science Team) Canyons incised into the southwest slope of Yega Volcano, northern Chad. Steep-walled channels incise into soft

Tarso Voon ignimbrites revealing more resistant basement schists. Channels are the result of groundwater seepage and surface runoff during infrequent storms or previous eras of wetter climate. Canyons can be seen to form a dendritic pattern similar to those observed on Mars. This image was acquired on 12 Jan 2003, covers an area of 51 x 54 km, and is centered near 20.3°N, 17.1°E. Image downloaded from: http://asterweb.jpl.nasa.gov/gallery-detail.asp?name=tibesti.

Figure 7 Compilation of faults, drainage channels and impact ejecta mapped in the study area.

Figure 8 Context map illustrating the location of the following local maps. Context map as well as local maps are all processed in ArcGIS.

Figure 8a An example of various fault fragments interpreted to belong to the same generation due to contact. Top of figure is north. Green arrow indicates direction of sun illumination.

Figure 8b An example of faults near the summit of Alba Patera not cross-cut by any other feature, implying an unknown in age. Top of figure is north. Green arrow indicates direction of illumination.

Figure 8c An example of sediment deposition at the point of confluence of a tributary (dark blue) to a main drainage channel (light blue) implying that the older tributary is older. Top of figure is north. Green arrow indicates direction of illumination. Blue arrows indicate channel flow direction.

Figure 8d An example of disconnected drainage channels not cross cut by any other feature which are designated as 1st generation channels (dark blue). Top of figure is north. Green arrow indicates direction of illumination. Blue arrows indicate channel flow direction.

Figures 8e-r Examples of cross cutting interpretations described in detail in section 3.1. Top of all figures is north. Green arrow indicates direction of illumination. Blue arrows indicate channel flow direction.

Figure 9 All 1091 craters mapped within study area to calculate the age of the surface. Craters mapped in ArcGIS using CraterTools toolbar (Kneissl et al., 2011). Graph shows size-frequency distribution of mapped craters, processed in Craterstats2 (Michael et al. 2011). Solid line illustrates the best cumulative fit isochron to data, indicating an age of ~ 2.89 Ga, + 0.32/-0.55 Ga to ~ 701 Ma, +/- 35 Ma.

Figure 10 1026 Craters in south section of mapped area mapped in ArcGIS using CraterTools toolbar (Kneissl et al., 2011). Graph shows size-frequency distribution of mapped craters, processed in Craterstats2 (Michael et al. 2011). Solid line illustrates the best cumulative fit isochron to data, indicating an age of ~ 3.24 Ga, +0.17/-0.60 Ga to ~ 885 Ma, +46/-47 Ma.

Figure 11 65 Craters in south section of mapped area mapped in ArcGIS using CraterTools toolbar (Kneissl et al., 2011). Graph shows size-frequency distribution of mapped craters, processed in Craterstats2

(Michael et al. 2011). Solid line illustrates the best cumulative fit isochron to data, indicating an age of ~ 2.49 Ga, +0.65/-0.82 Ga to ~ 678 Ma, +/- 100 Ma.

Figure 12 Profile of MOLA topography data along a SSE-NNW transect within the study region. Topography above ~ 1500 m is concave downward indicating an erosional setting and topography below ~ 1500 m is concave upward, possibly indicating a depositional setting.

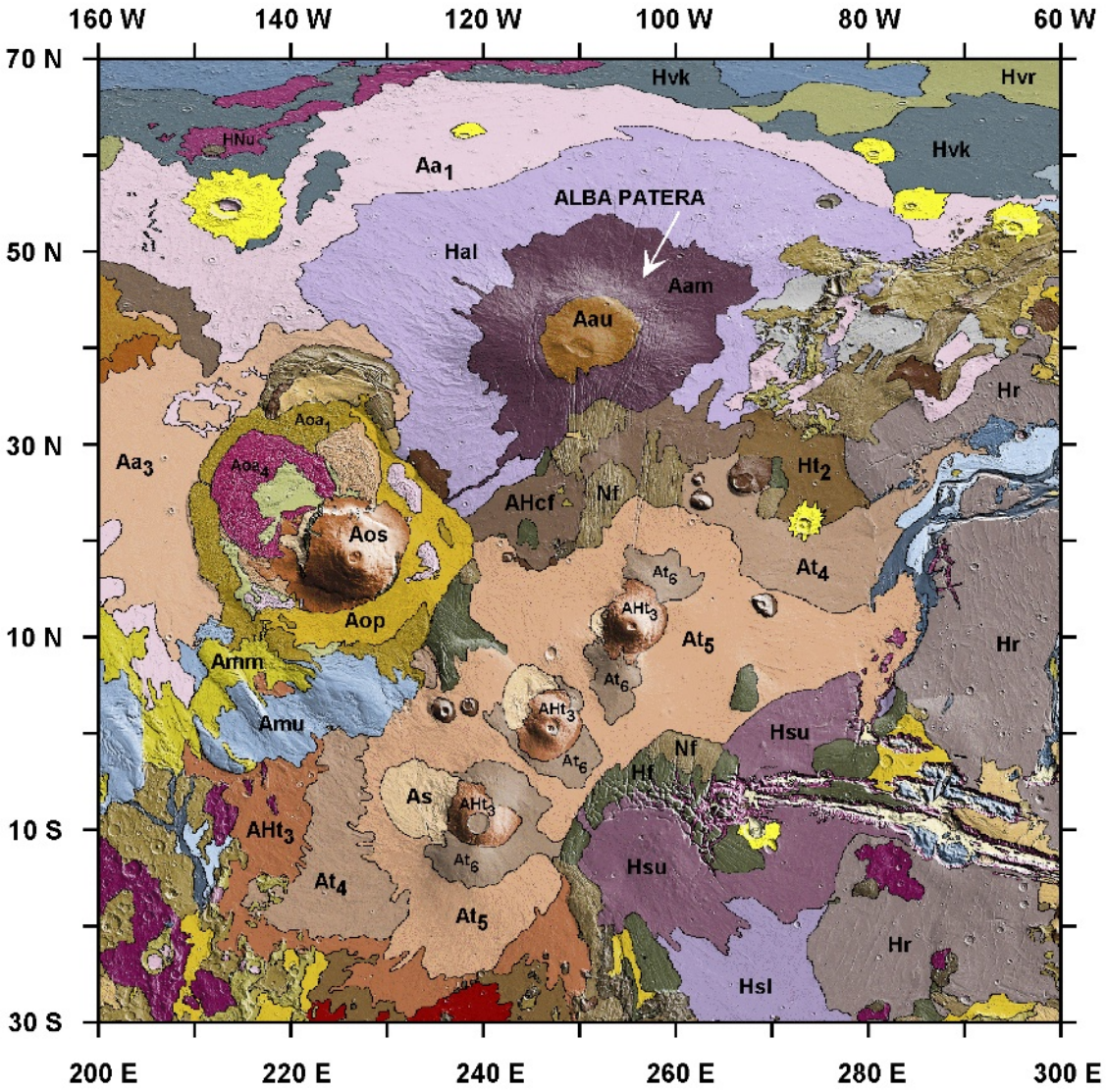
160 W
140 W
120 W
100 W
80 W
60 W
70 N
50 N
30 N
10 N
10 S
30 S
200 E
220 E
240 E
260 E
280 E
300 E
Hvk
Hvr
HNu
Aa1
ALBA PATERA
Hal
Aam
Aau
Hr
Aoa1
Aa3
Aoa4
Ht2
AHcf
Nf
Aos
At4
At6
AHt3
At5
Aop
Amm
Amu
Hsu
As
Hf
At4
At5
Hsl

Figure 1

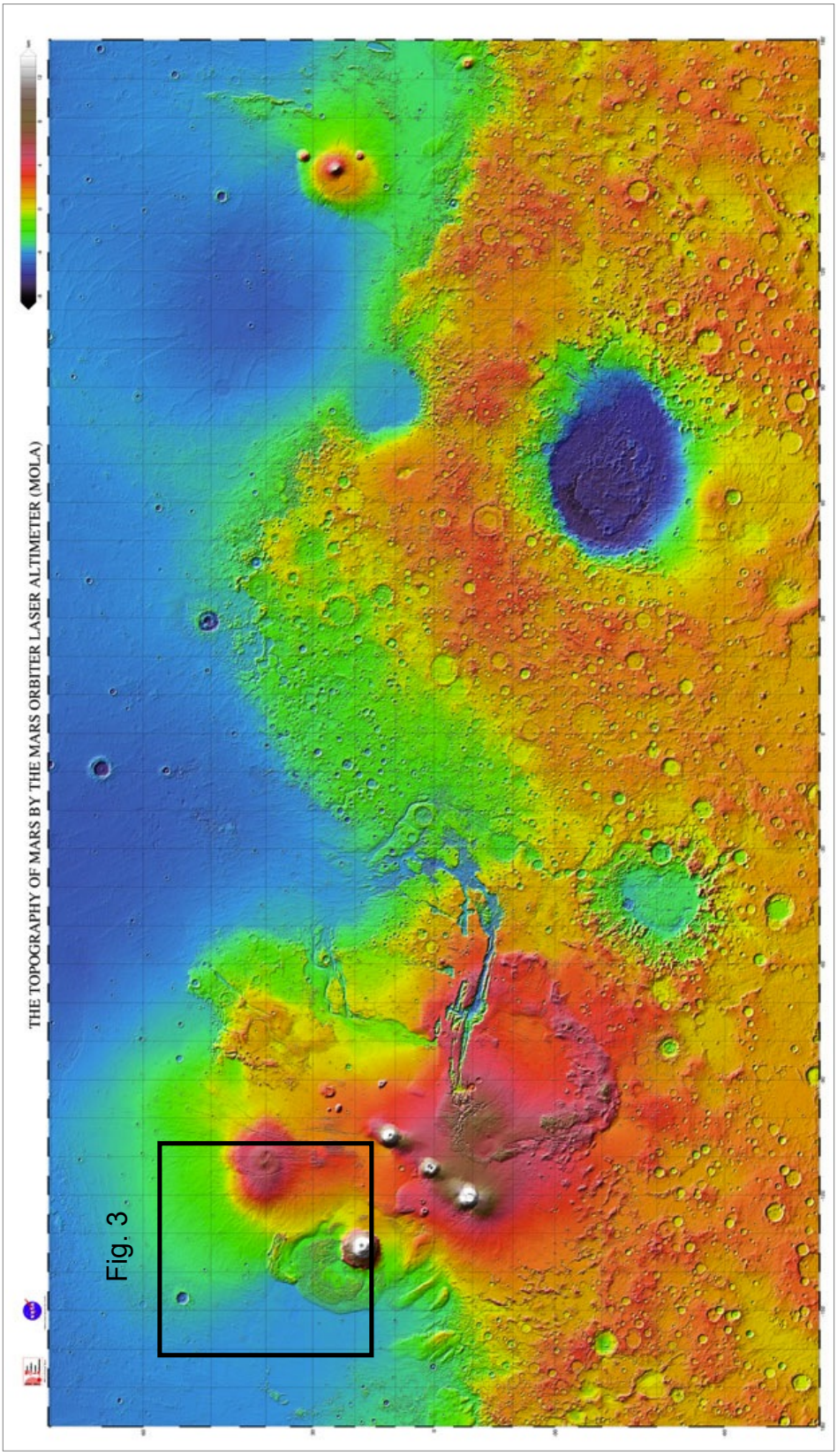
THE TOPOGRAPHY OF MARS BY THE MARS ORBITER LASER ALTIMETER (MOLA)
Fig. 3

Figure 2

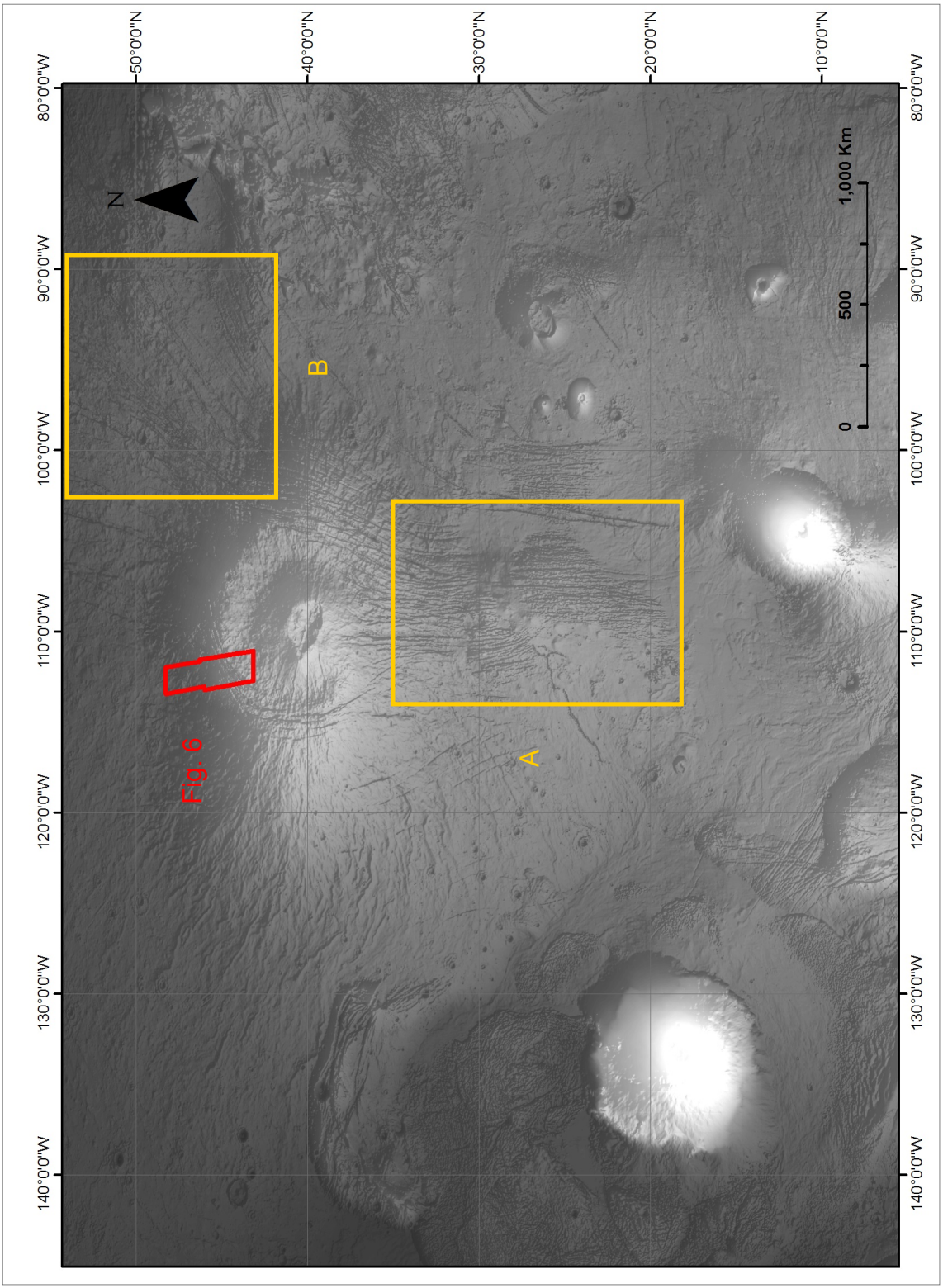
50°0'0"N
40°0'0"N
30°0'0"N
20°0'0"N
10°0'0"N
80°0'0"W
90°0'0"W
100°0'0"W
110°0'0"W
120°0'0"W
130°0'0"W
140°0'0"W
N
B
A
Fig. 6
0
500
1,000 Km

Figure 3

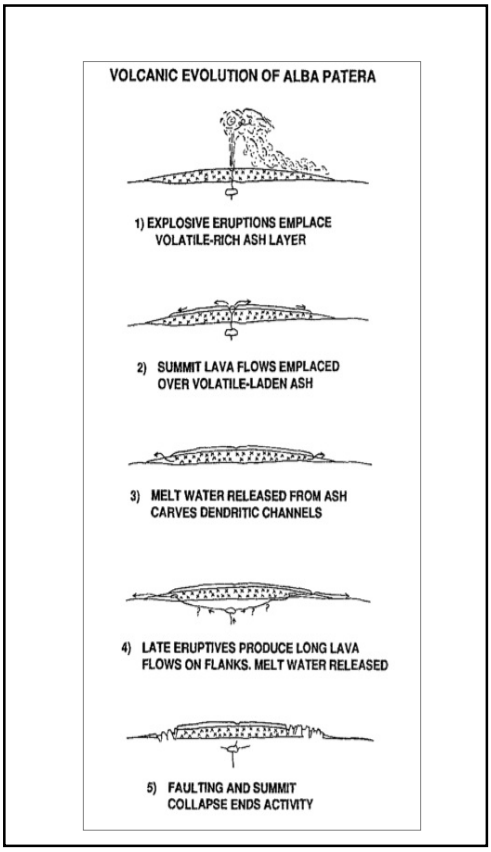

Figure 4

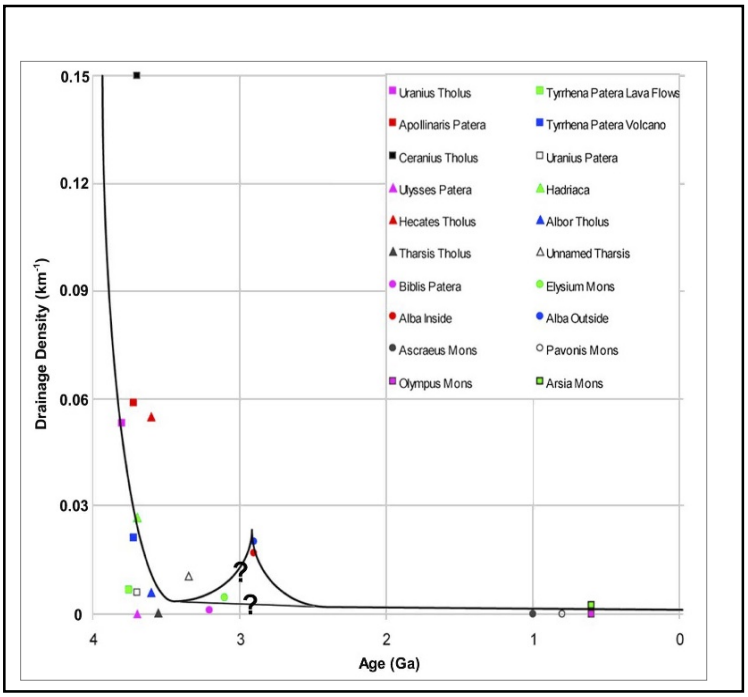

Figure 5

Figure 6

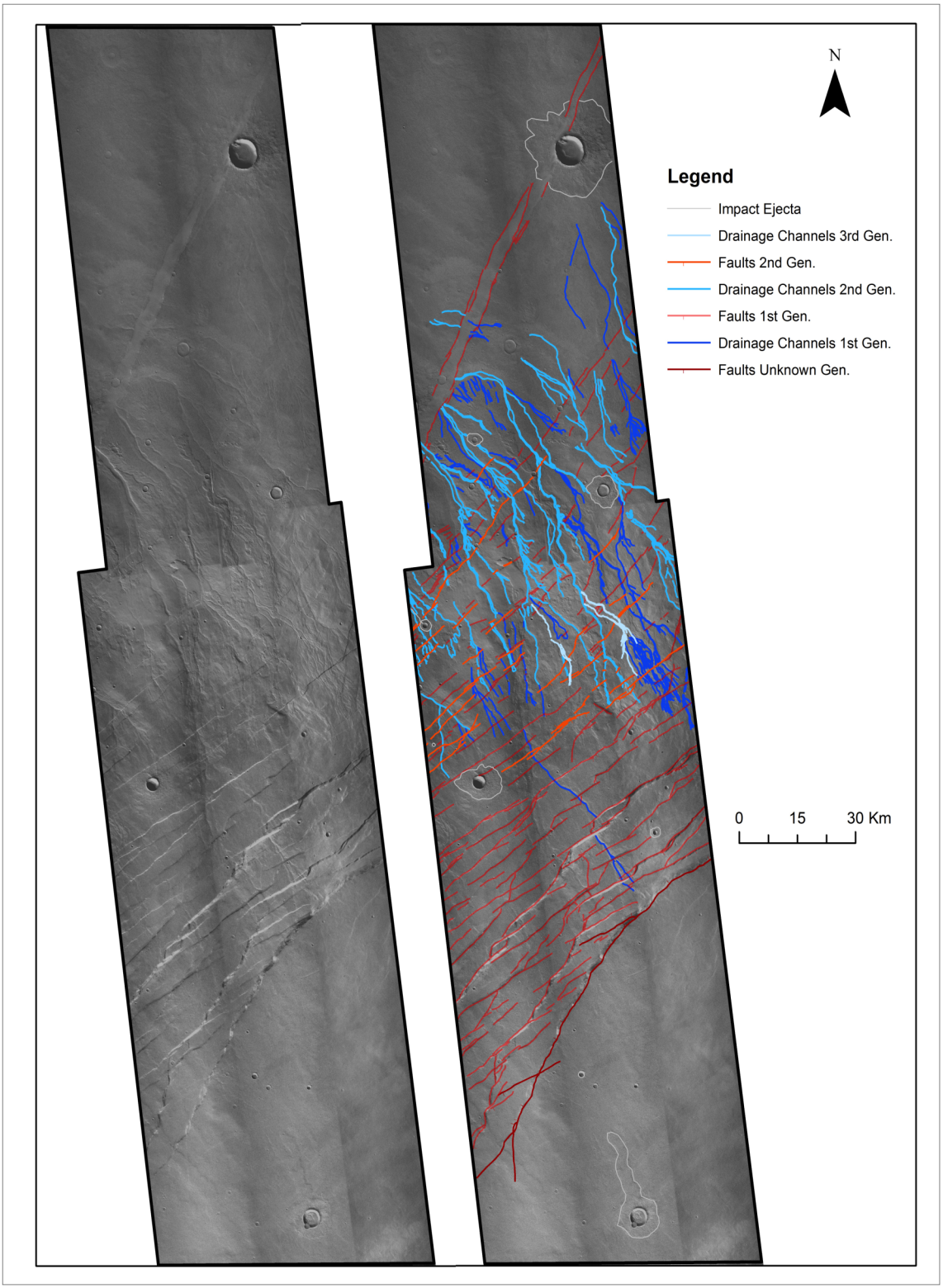
N
Legend
Impact Ejecta
Drainage Channels 3rd Gen.
Faults 2nd Gen.
Drainage Channels 2nd Gen.
Faults 1st Gen.
Drainage Channels 1st Gen.
Faults Unknown Gen.
0
15
30 Km

Figure 7

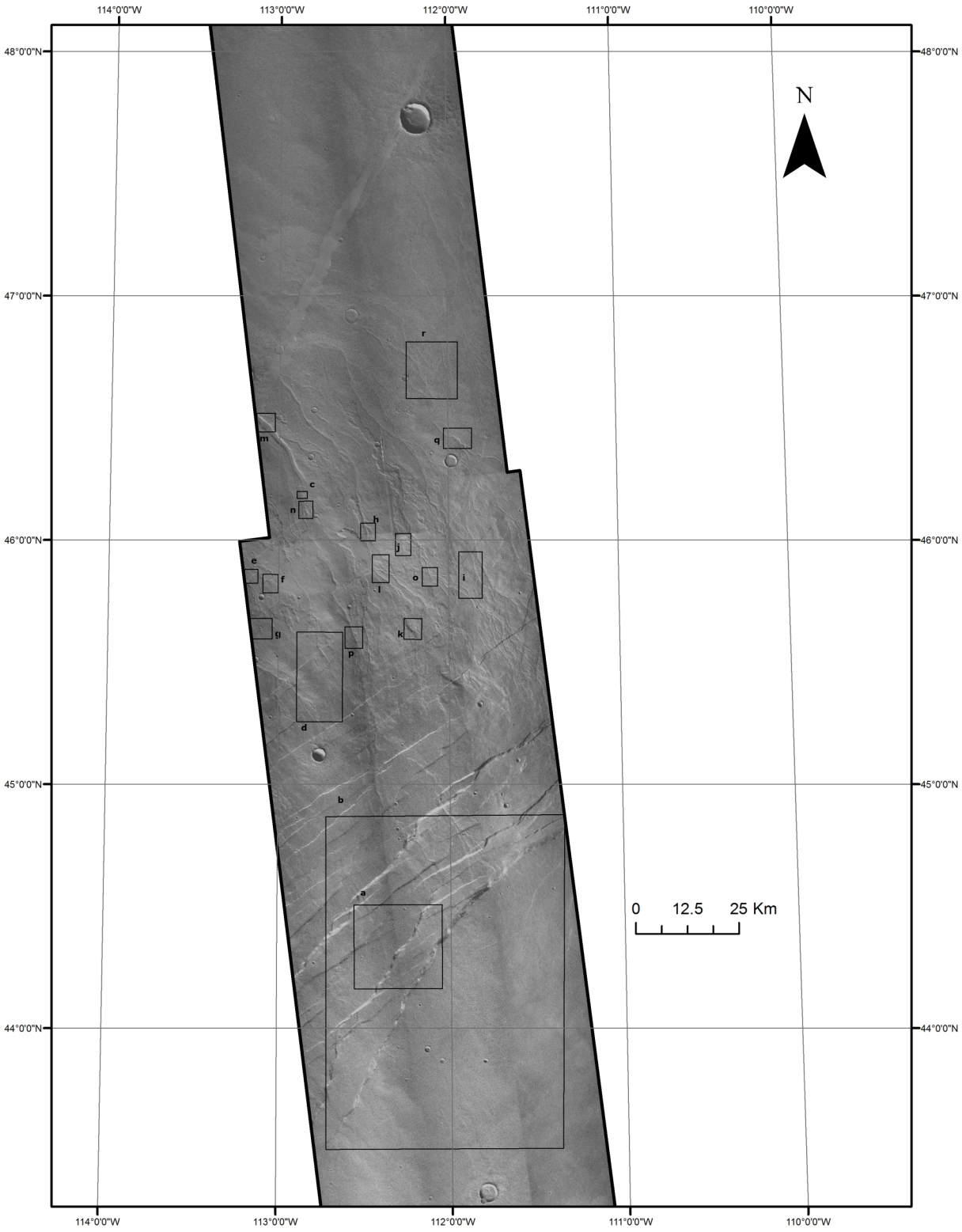
114°0'0"W
113°0'0"W
112°0'0"W
111°0'0"W
110°0'0"W
48°0'0"N
47°0'0"N
46°0'0"N
45°0'0"N
44°0'0"N
N
0 12.5 25 Km
a
b
c
d
e
f
g
h
i
j
k
l
m
n
o
p
q
r

Figure 8

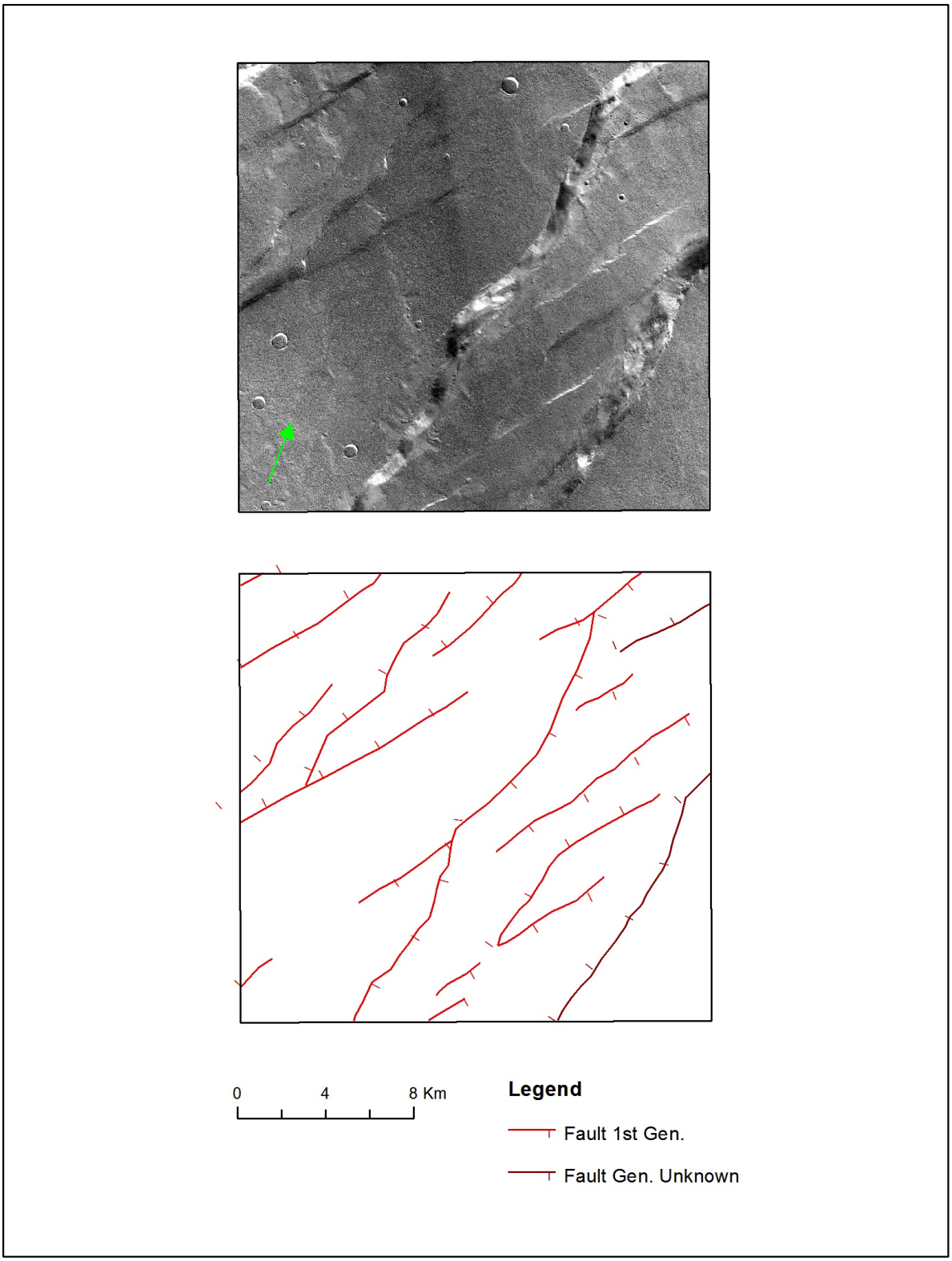

Figure 8a

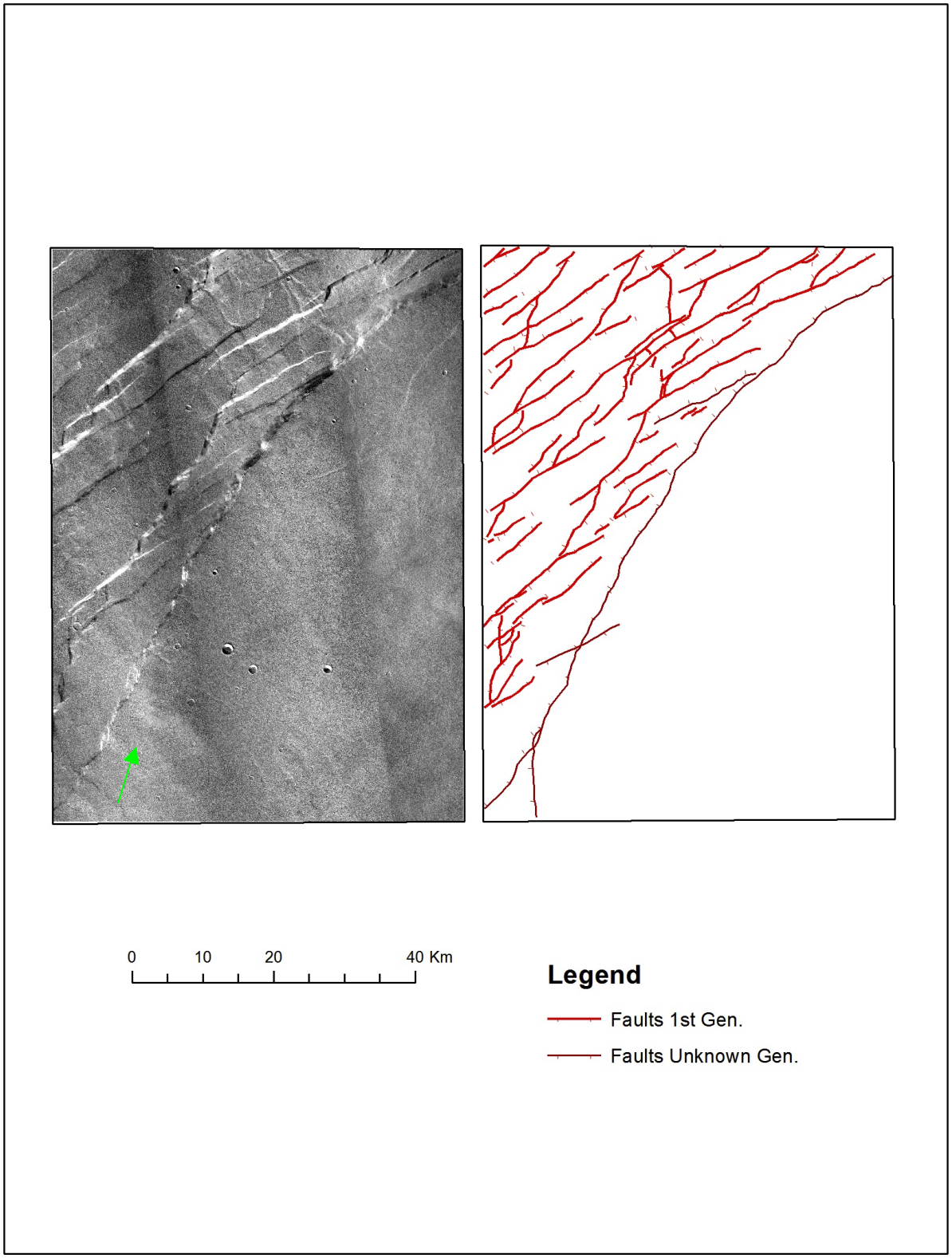

Figure 8b

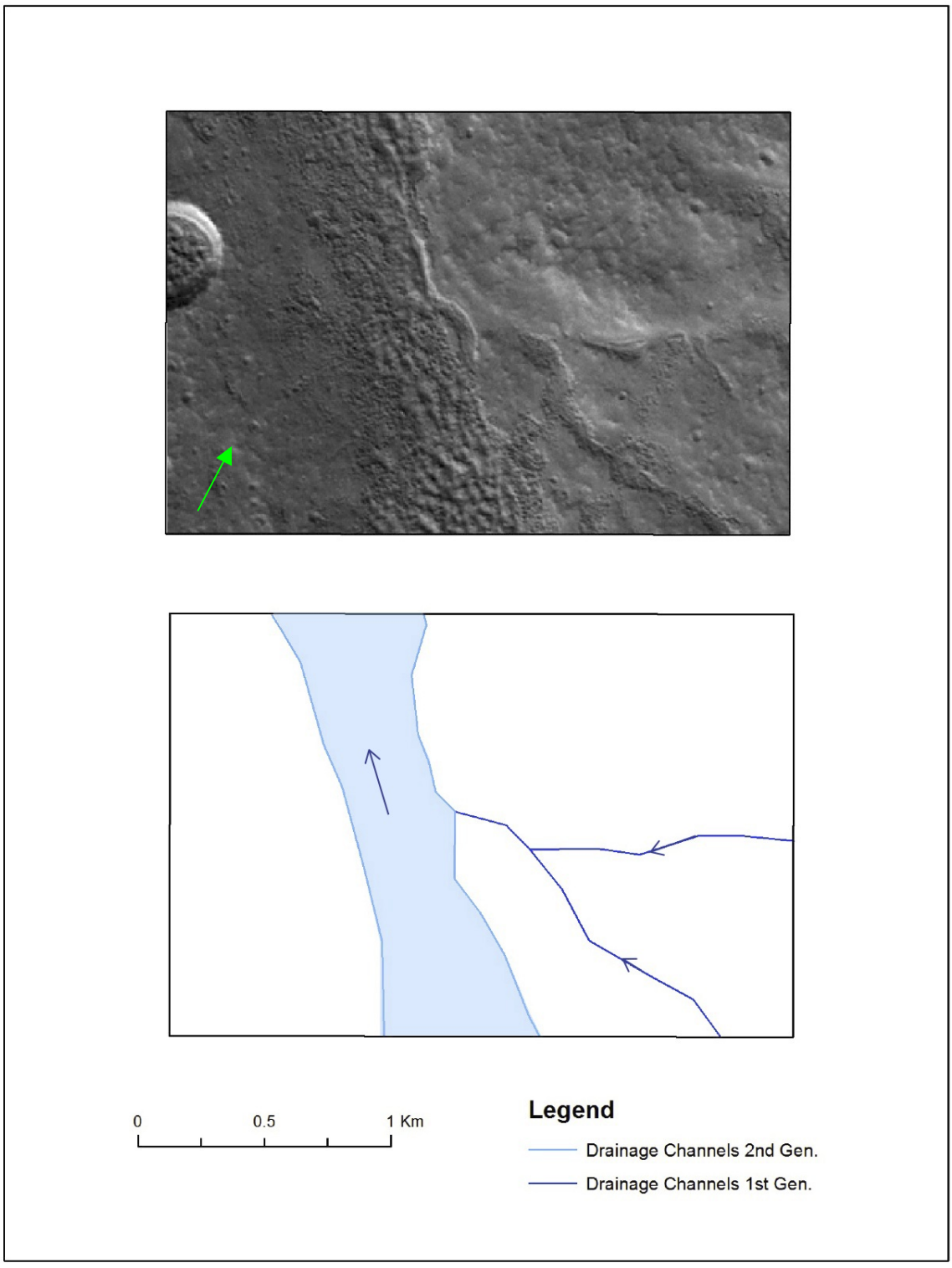
0
0.5
1 Km
Legend
Drainage Channels 2nd Gen.
Drainage Channels 1st Gen.

Figure 8c

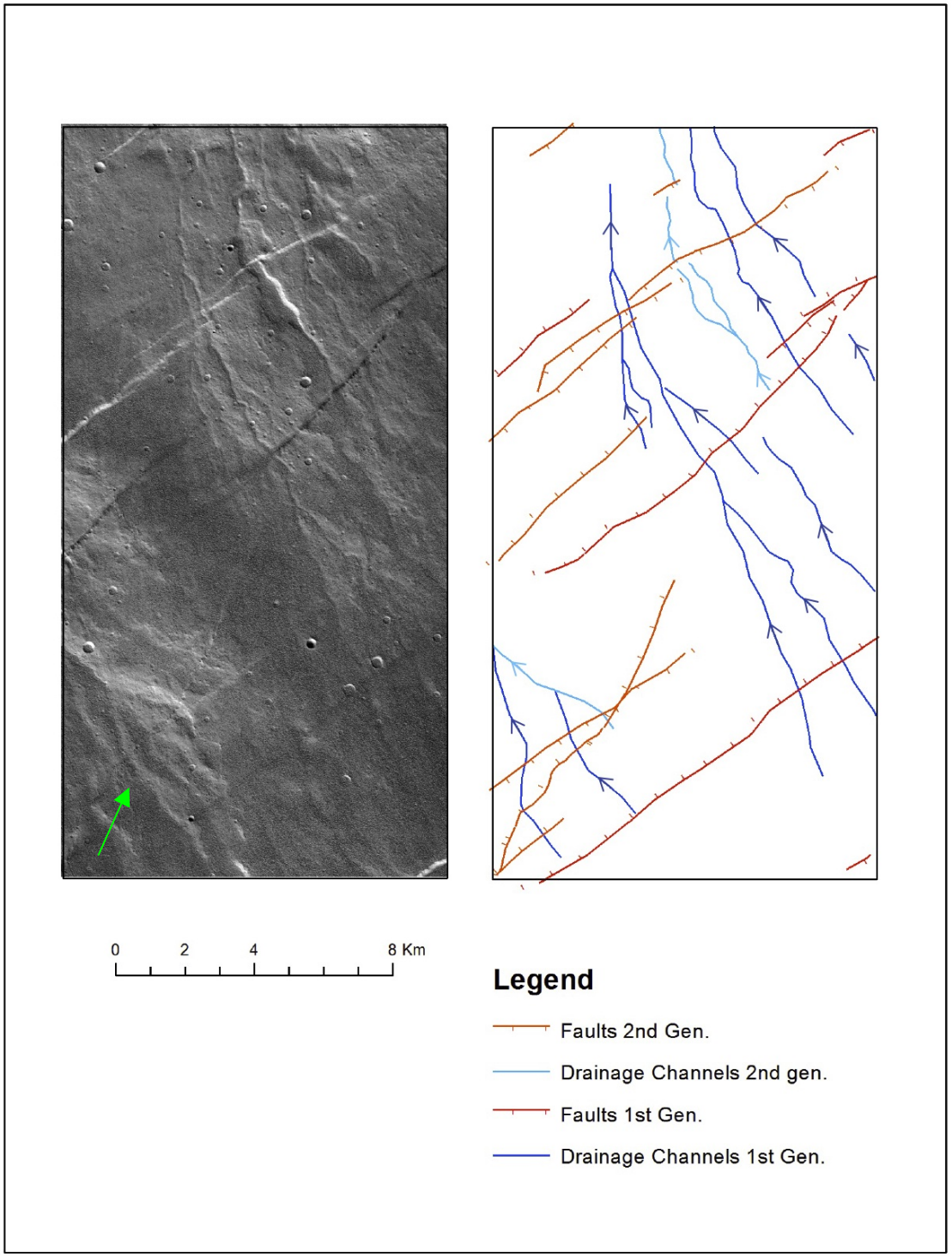
0
2
4
8 Km
Legend
Faults 2nd Gen.
Drainage Channels 2nd gen.
Faults 1st Gen.
Drainage Channels 1st Gen.

Figure 8d

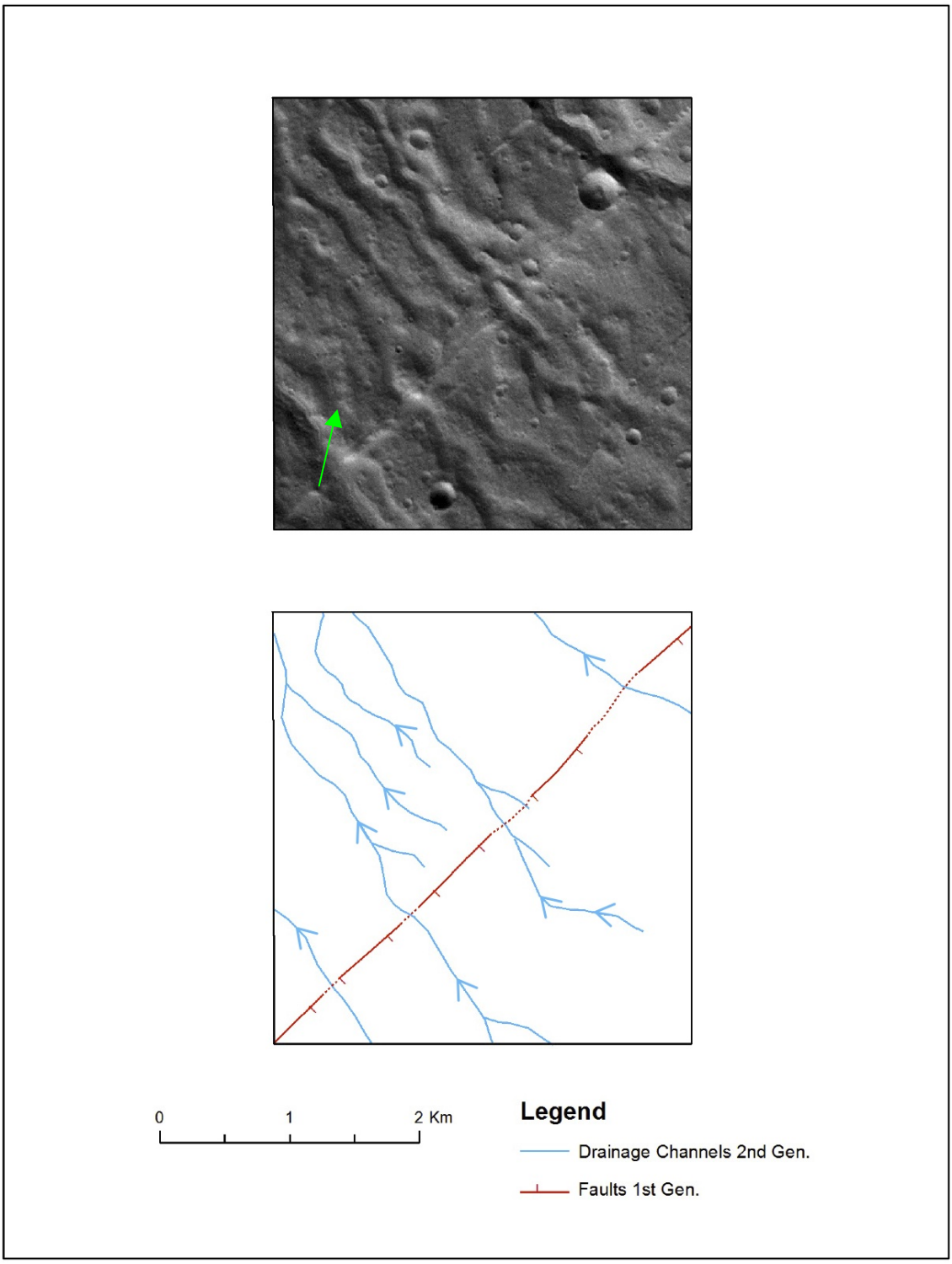

Figure 8e

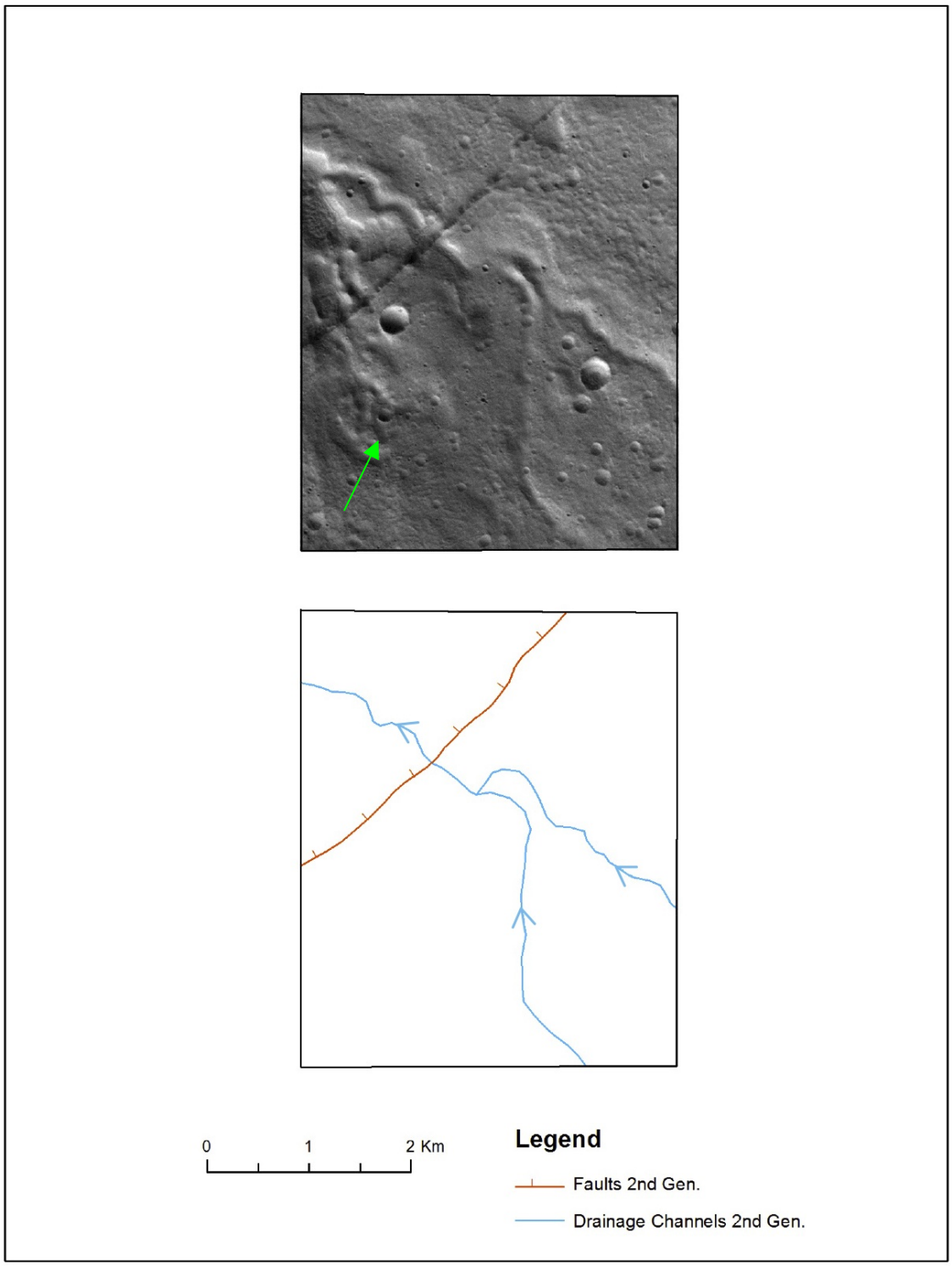

Figure 8f

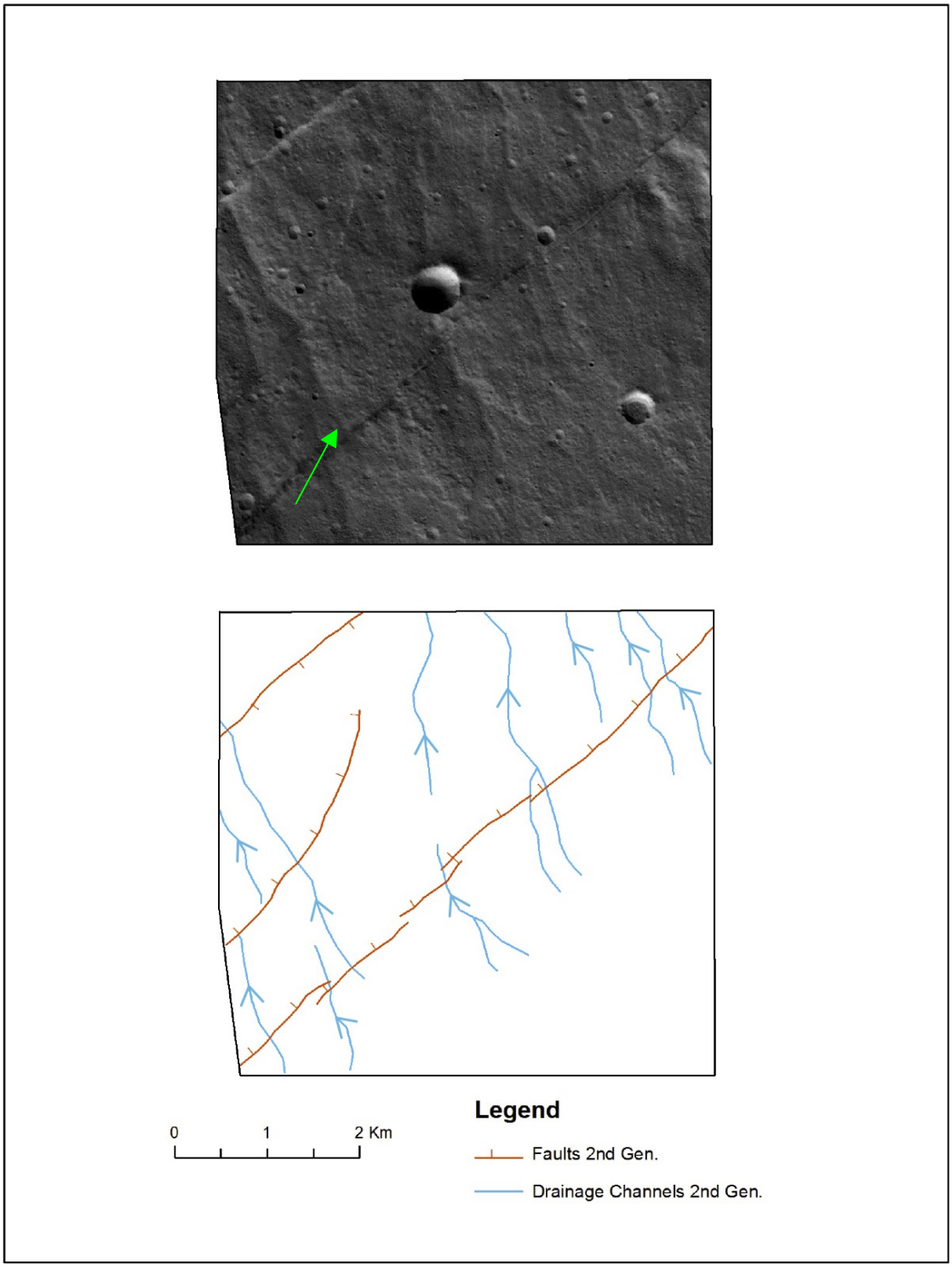

Figure 8g

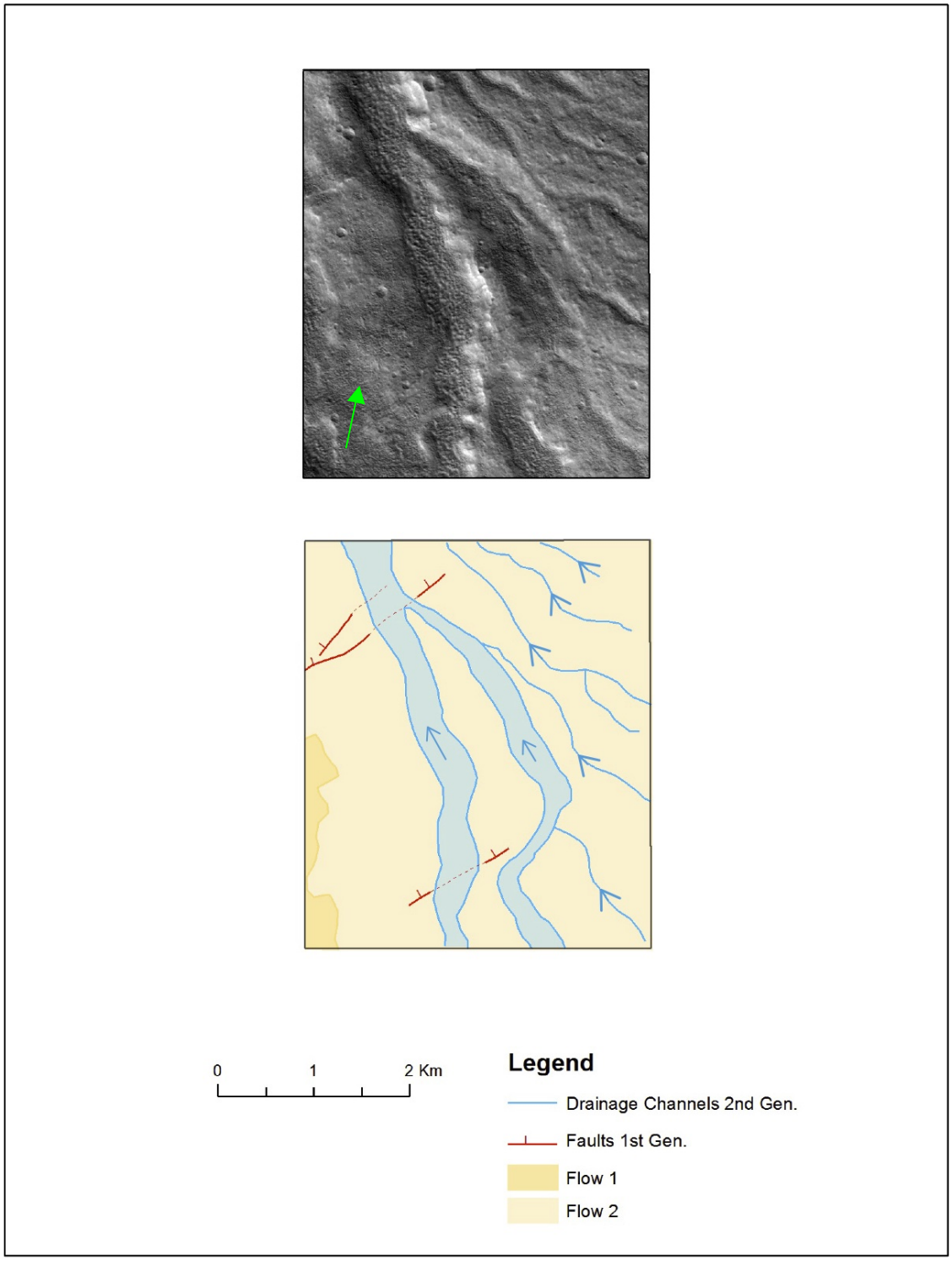
0
1
2 Km
Legend
Drainage Channels 2nd Gen.
Faults 1st Gen.
Flow 1
Flow 2

Figure 8h

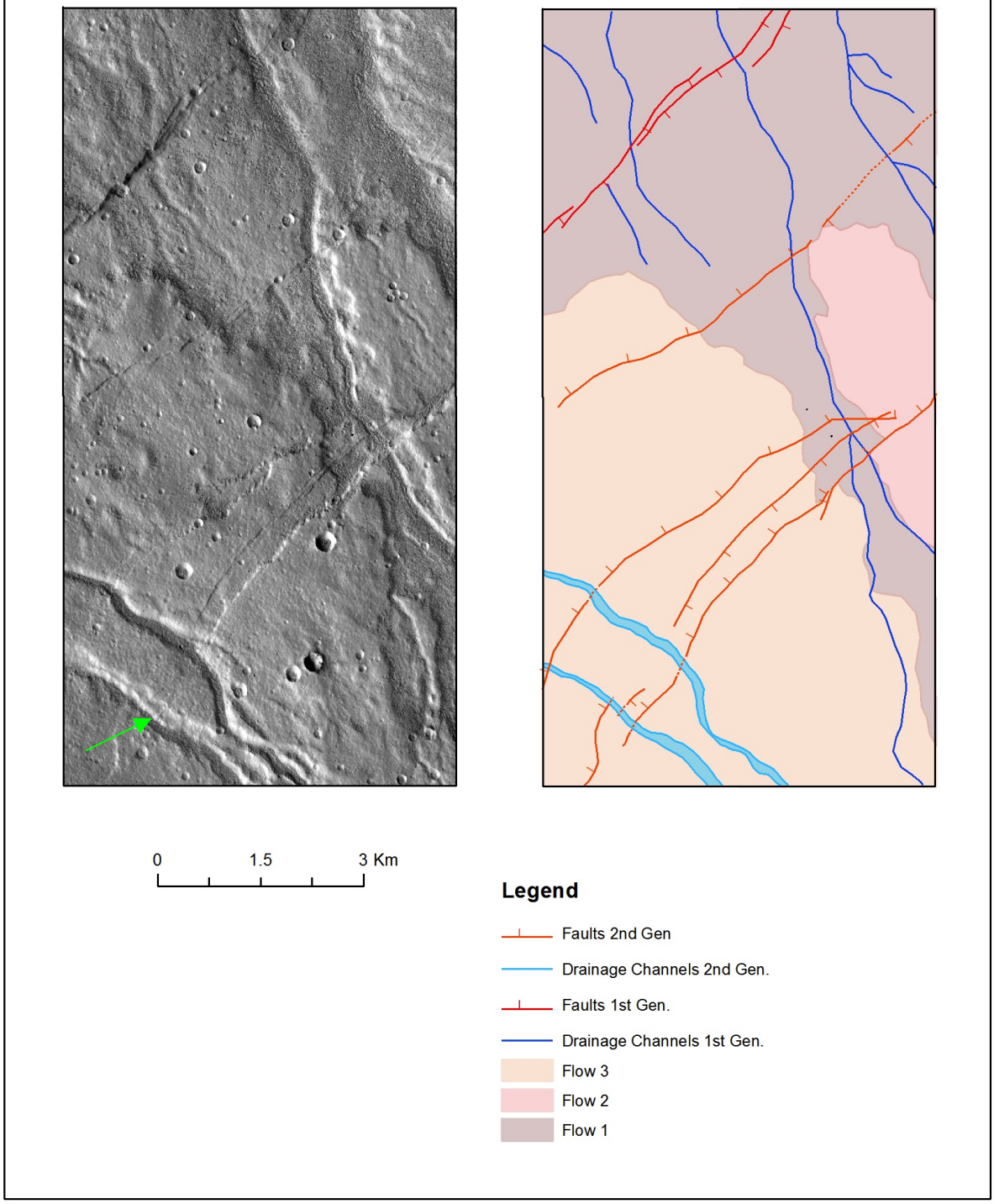
0
1.5
3 Km
Legend
Faults 2nd Gen
Drainage Channels 2nd Gen.
Faults 1st Gen.
Drainage Channels 1st Gen.
Flow 3
Flow 2
Flow 1

Figure 8i

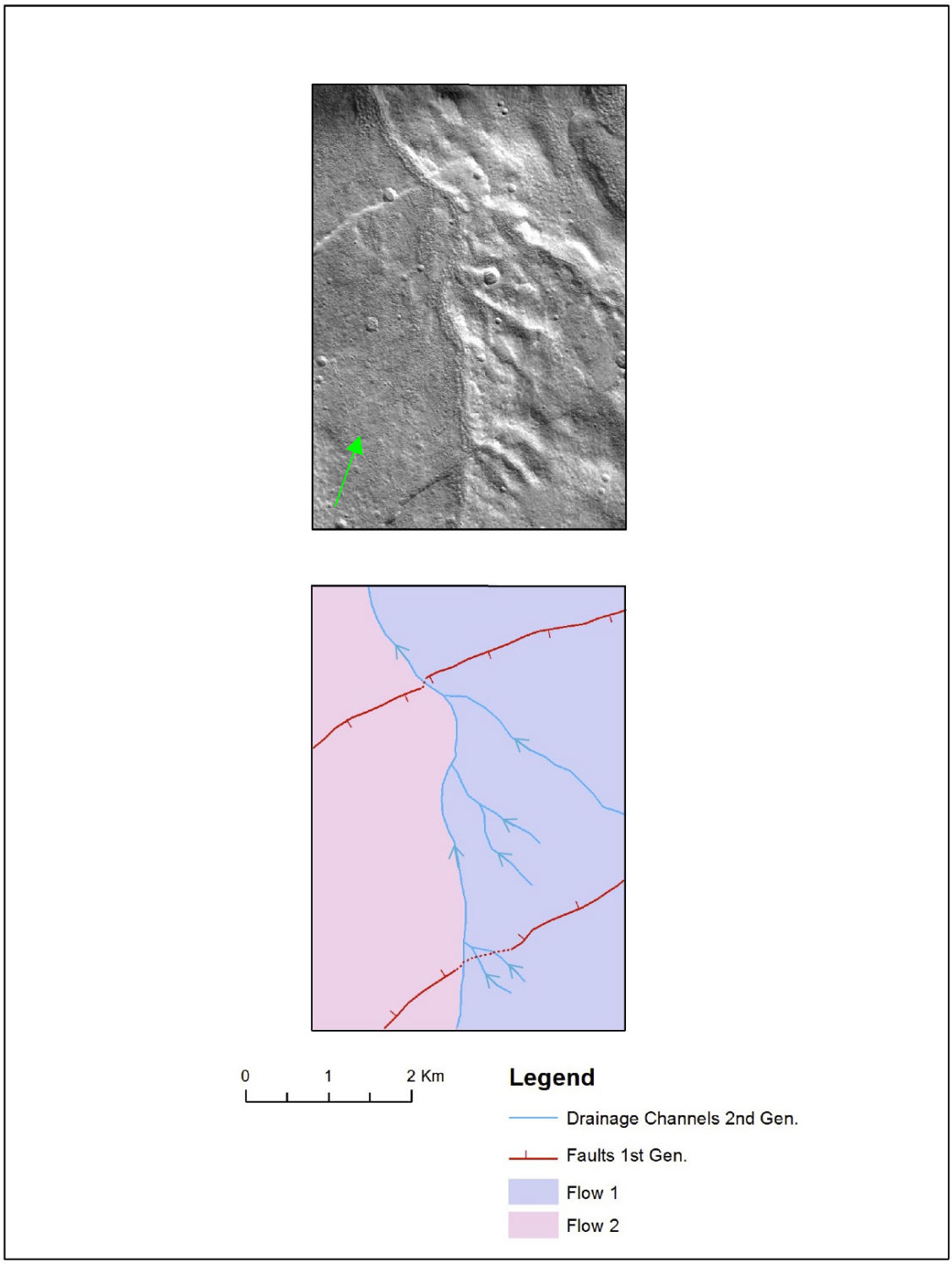
0
1
2 Km
Legend
Drainage Channels 2nd Gen.
Faults 1st Gen.
Flow 1
Flow 2

Figure 8j

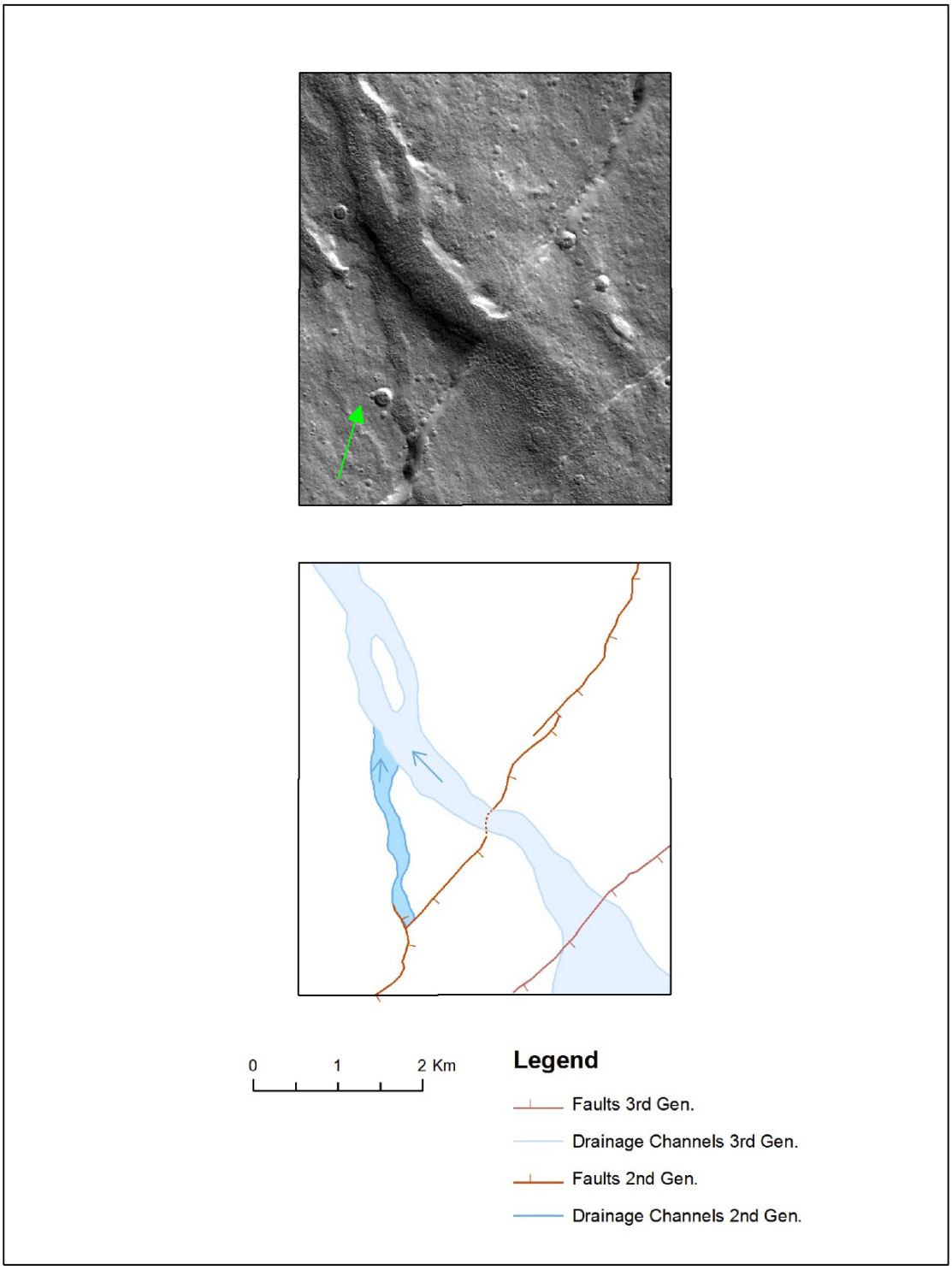
0
1
2 Km
Legend
Faults 3rd Gen.
Drainage Channels 3rd Gen.
Faults 2nd Gen.
Drainage Channels 2nd Gen.

Figure 8k

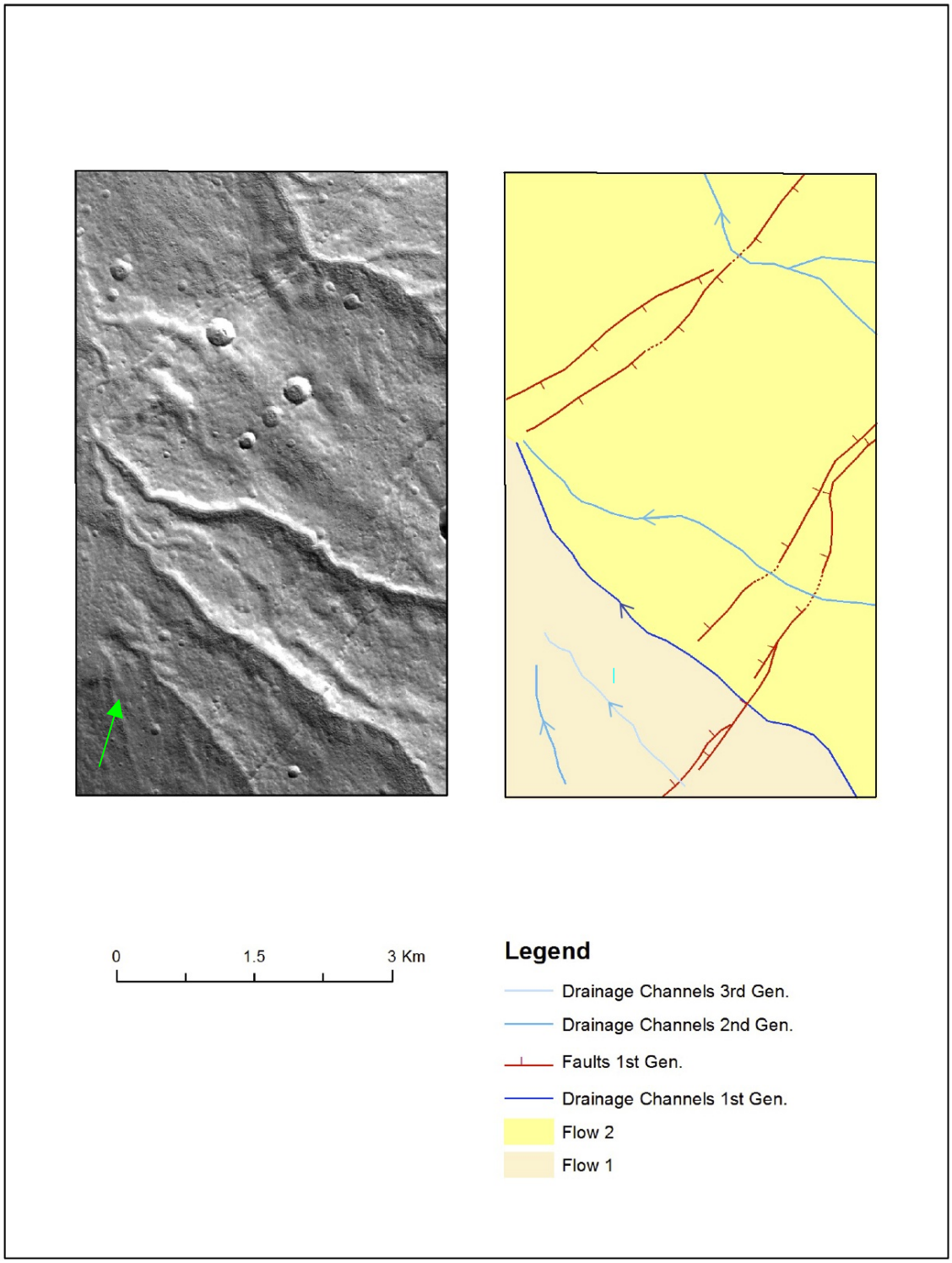
0
1.5
3 Km
Legend
Drainage Channels 3rd Gen.
Drainage Channels 2nd Gen.
Faults 1st Gen.
Drainage Channels 1st Gen.
Flow 2
Flow 1

Figure 8I

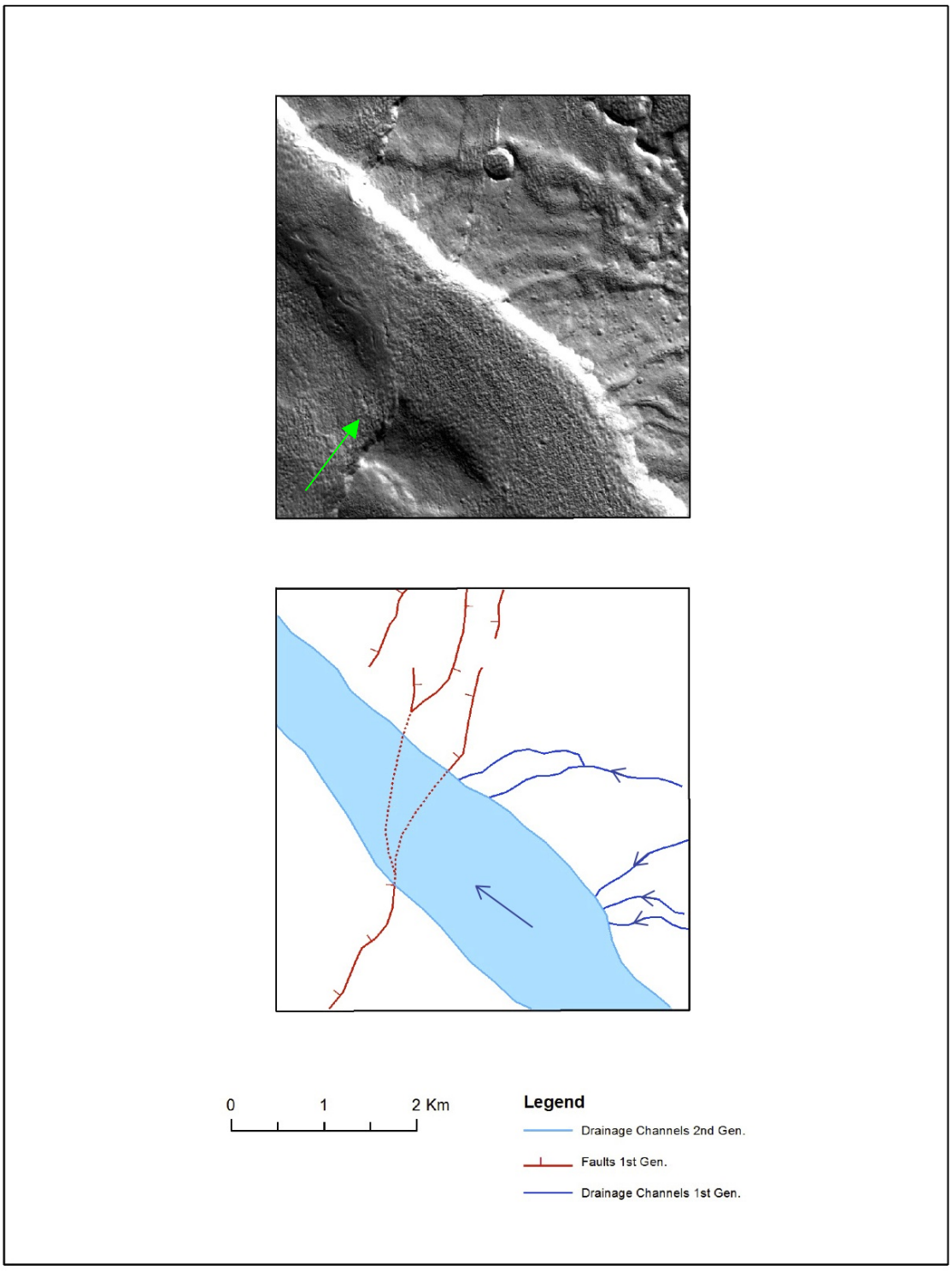
0
1
2 Km
Legend
Drainage Channels 2nd Gen.
Faults 1st Gen.
Drainage Channels 1st Gen.

Figure 8m

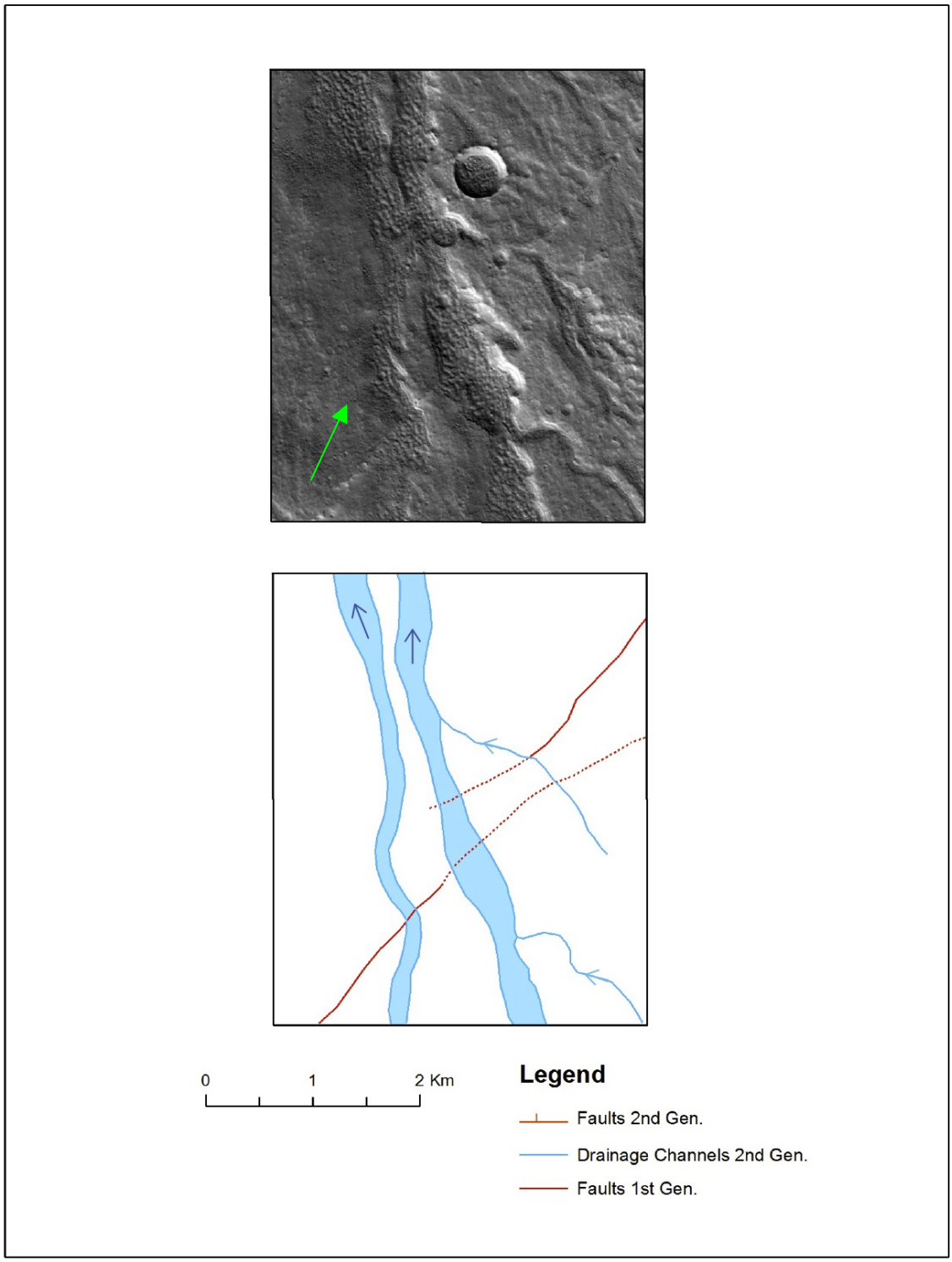
0
1
2 Km
Legend
Faults 2nd Gen.
Drainage Channels 2nd Gen.
Faults 1st Gen.

Figure 8n

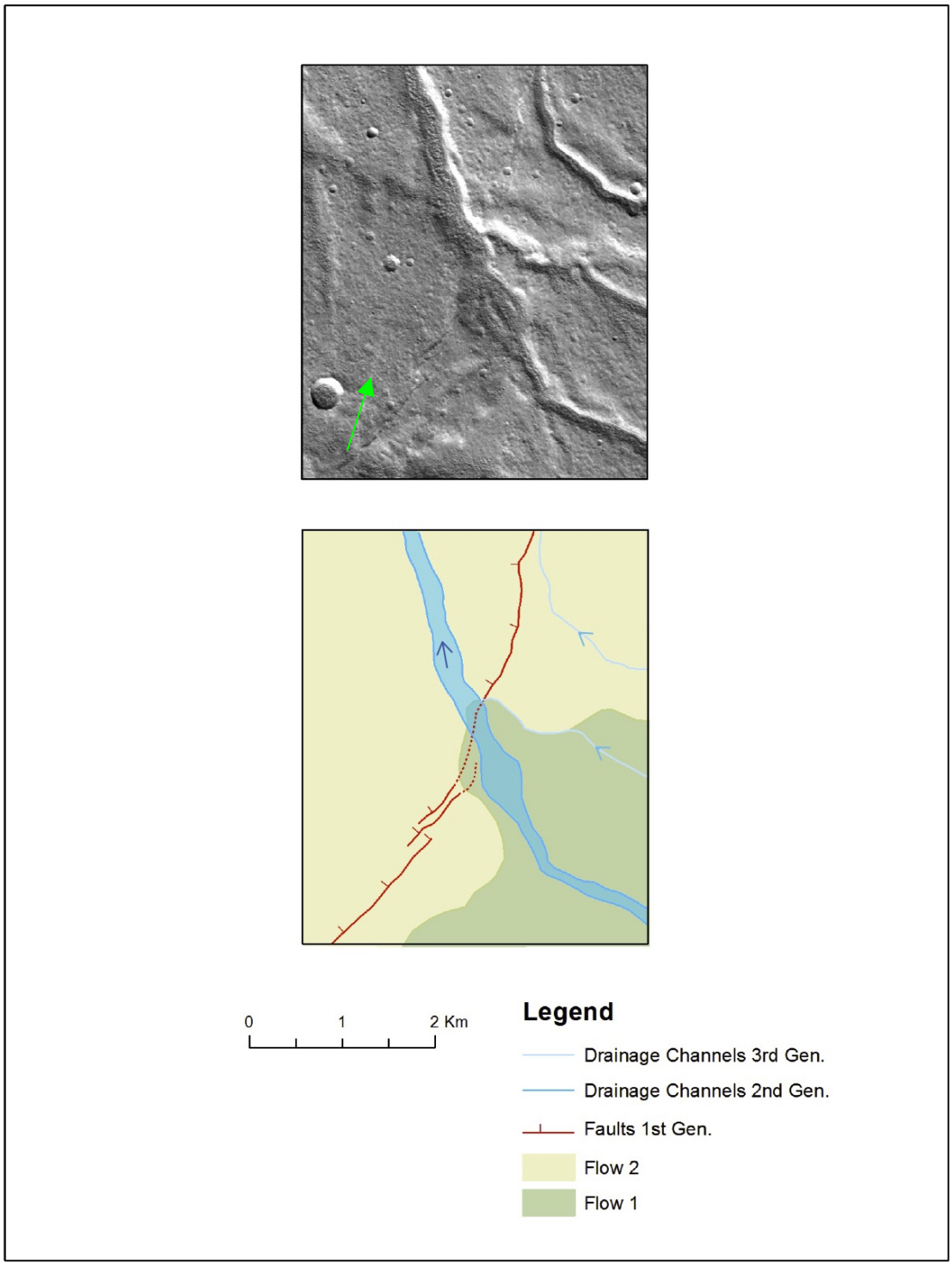
0
1
2 Km
Legend
Drainage Channels 3rd Gen.
Drainage Channels 2nd Gen.
Faults 1st Gen.
Flow 2
Flow 1

Figure 8o

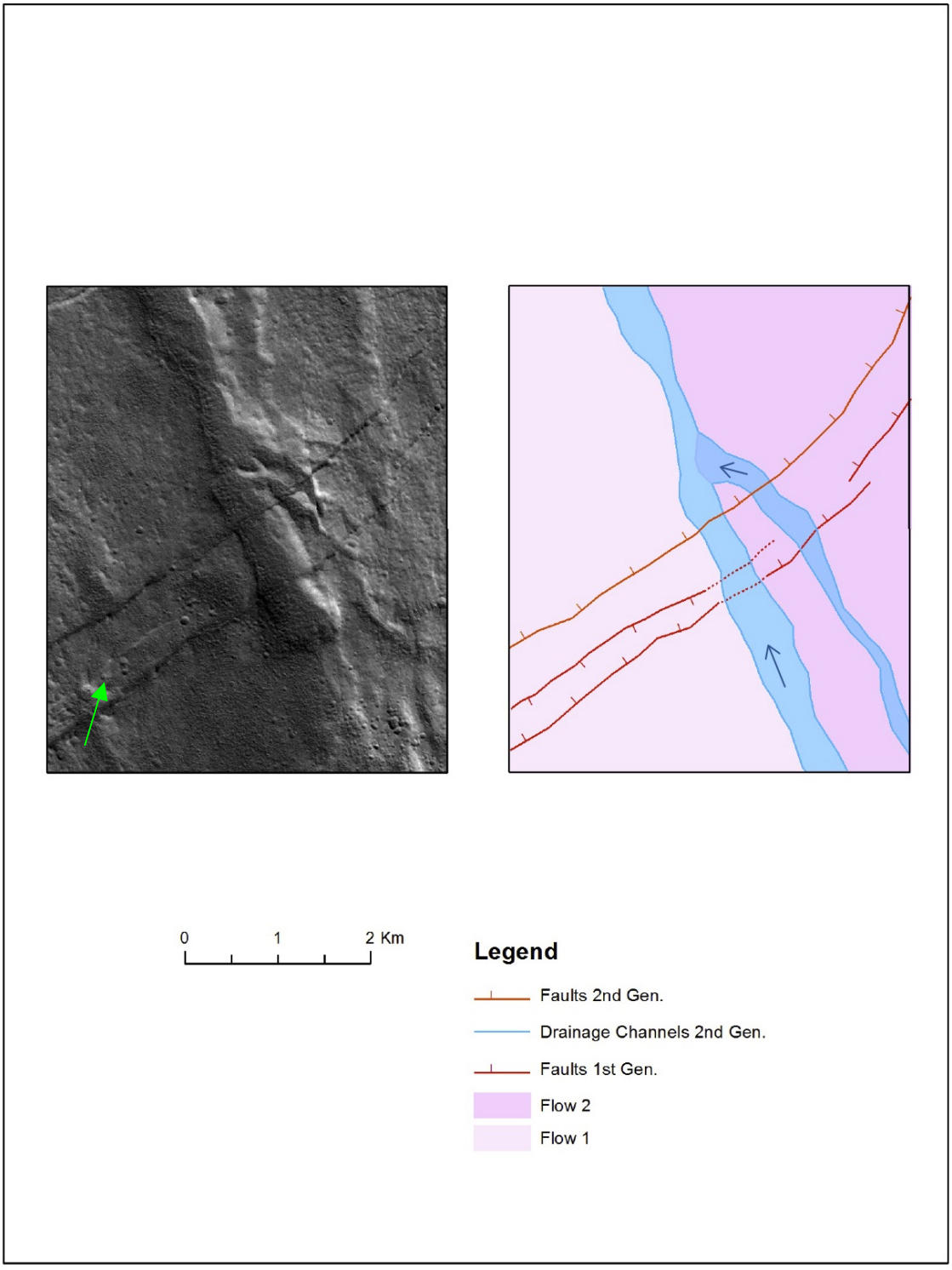
0
1
2 Km
Legend
Faults 2nd Gen.
Drainage Channels 2nd Gen.
Faults 1st Gen.
Flow 2
Flow 1

Figure 8p

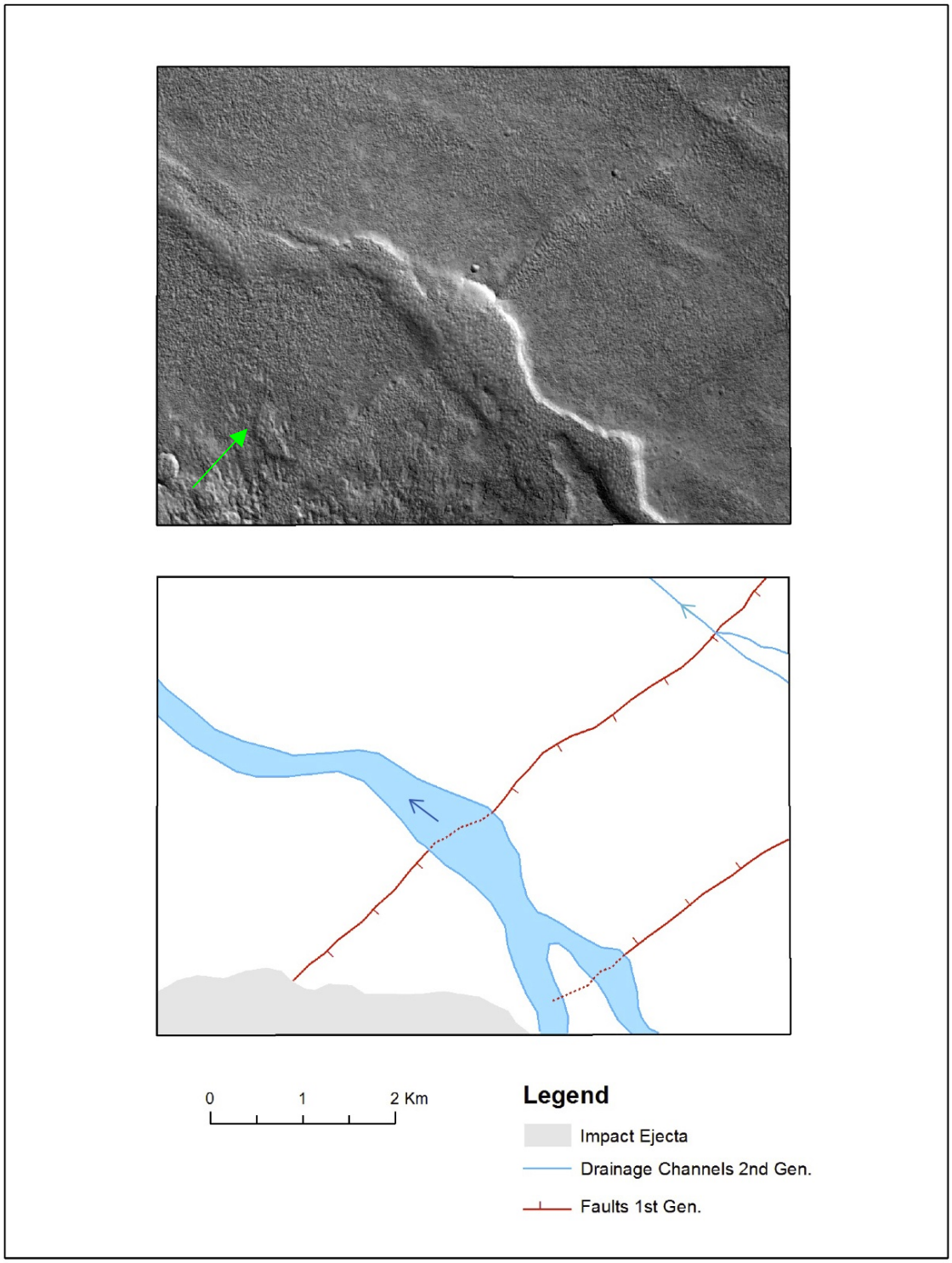
0
1
2 Km
Legend
Impact Ejecta
Drainage Channels 2nd Gen.
Faults 1st Gen.

Figure 8q

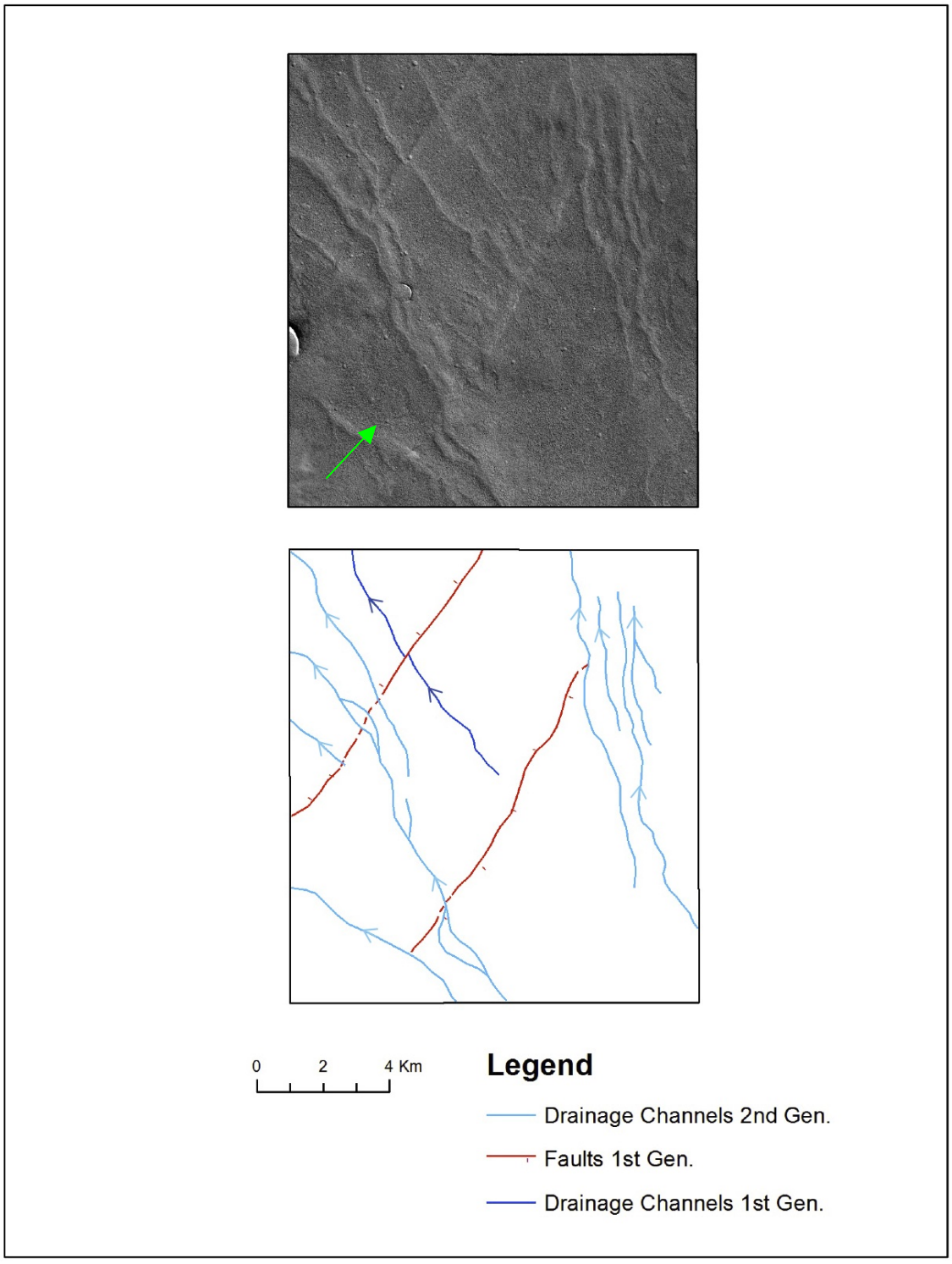
0
2
4 Km
Legend
Drainage Channels 2nd Gen.
Faults 1st Gen.
Drainage Channels 1st Gen.

Figure 8r

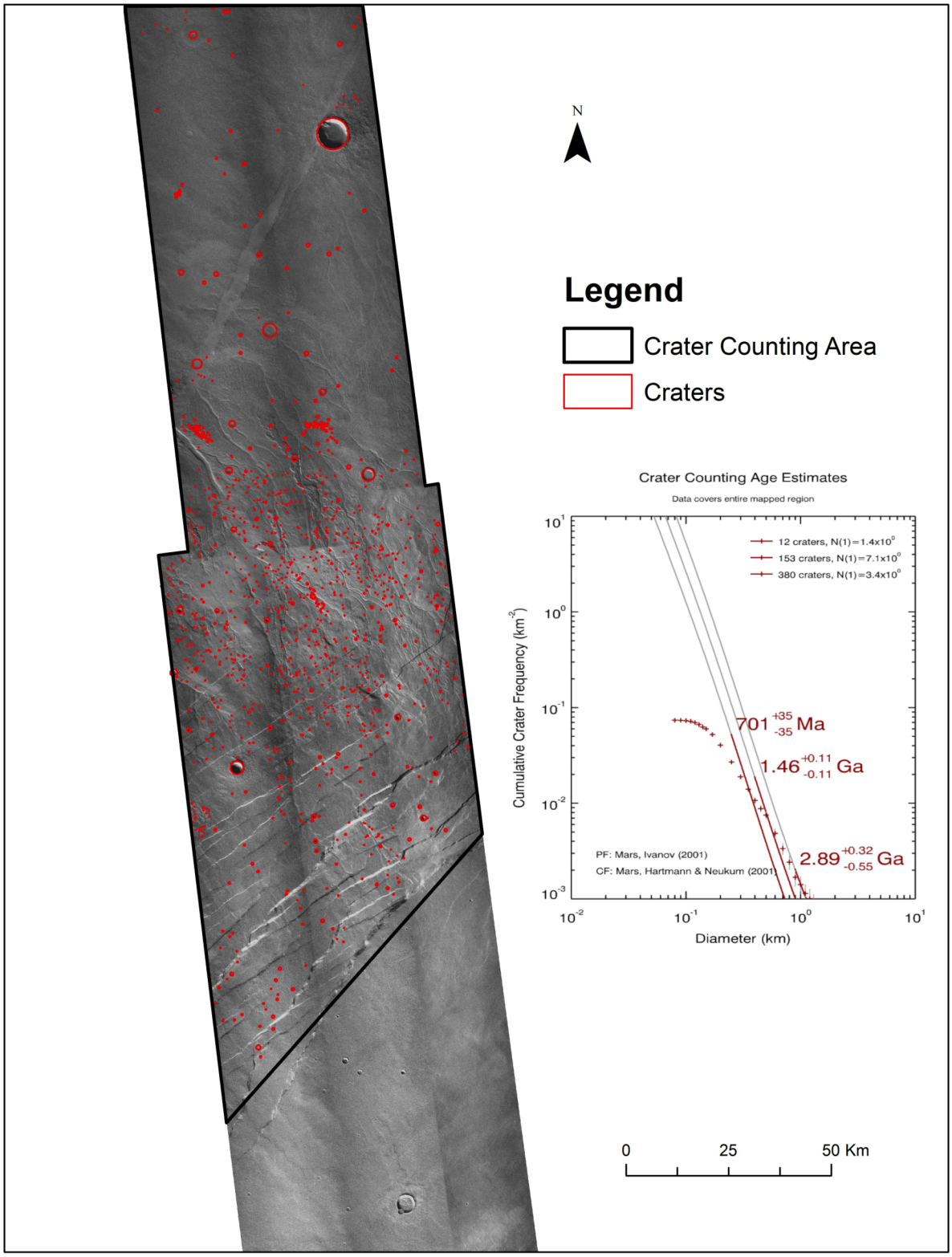
N
Legend
Crater Counting Area
Craters
Crater Counting Age Estimates
Data covers entire mapped region
12 craters, N(1)=1.4x10^0
153 craters, N(1)=7.1x10^0
380 craters, N(1)=3.4x10^0
701 +35 -35 Ma
1.46 +0.11 -0.11 Ga
2.89 +0.32 -0.55 Ga
PF: Mars, Ivanov (2001)
CF: Mars, Hartmann & Neukum (2001)
Cumulative Crater Frequency (km^-2)
Diameter (km)
0
25
50 Km

Figure 9

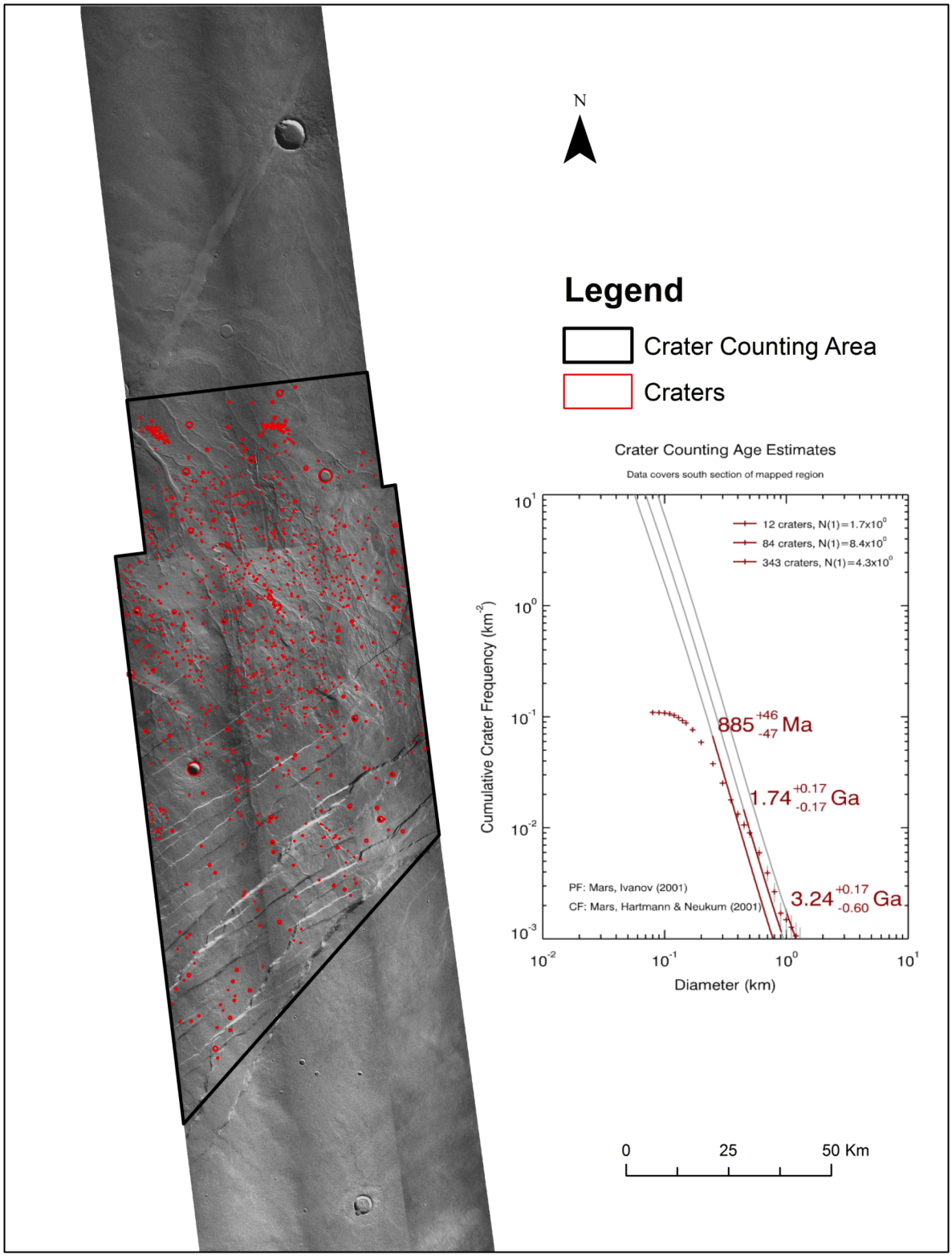
N
Legend
Crater Counting Area
Craters
Crater Counting Age Estimates
Data covers south section of mapped region
12 craters, N(1)=1.7x10^0
84 craters, N(1)=8.4x10^0
343 craters, N(1)=4.3x10^0
885 +46 -47 Ma
1.74 +0.17 -0.17 Ga
3.24 +0.17 -0.60 Ga
PF: Mars, Ivanov (2001)
CF: Mars, Hartmann & Neukum (2001)
Cumulative Crater Frequency (km^-2)
Diameter (km)
0
25
50 Km

Figure 10

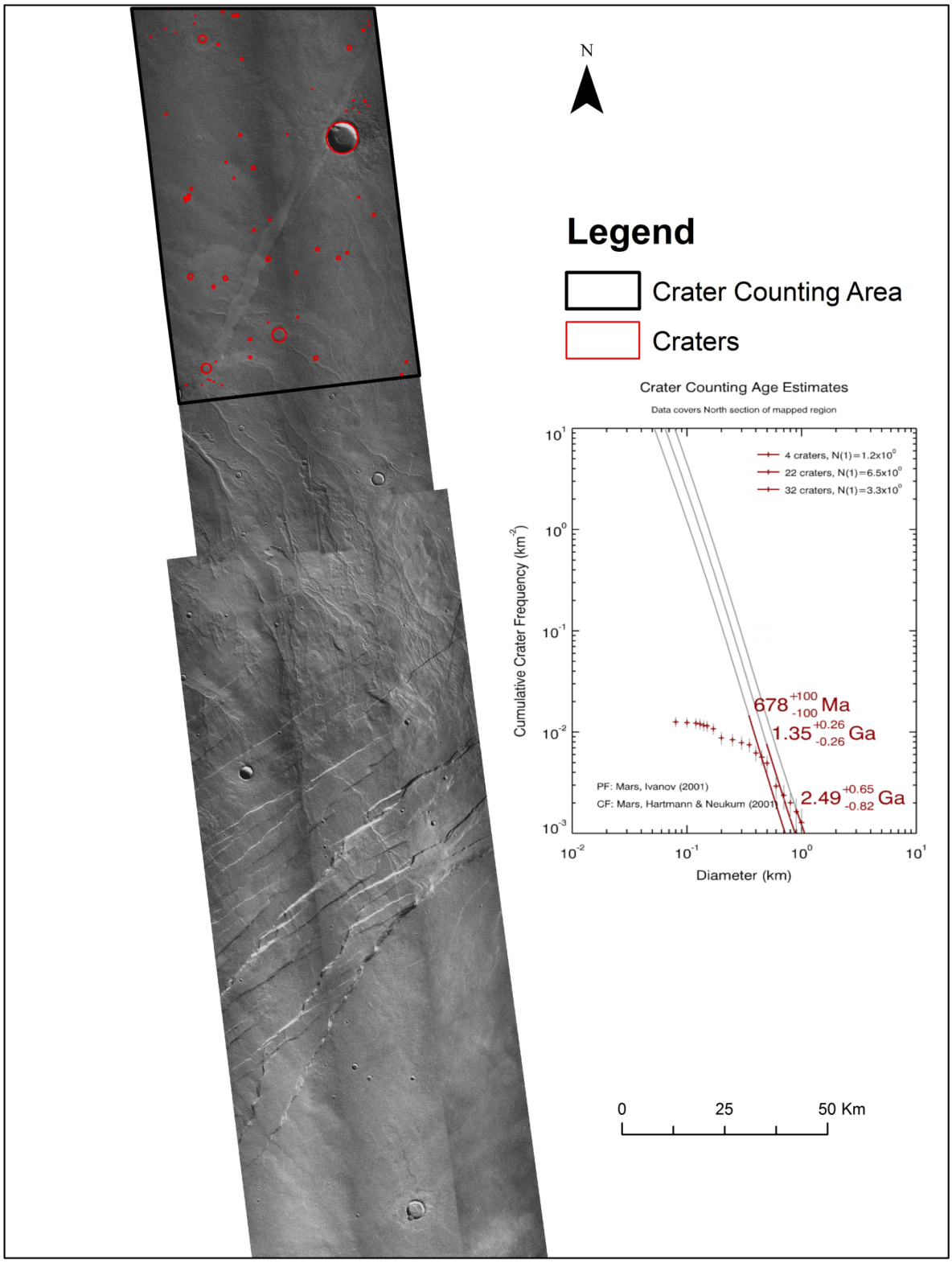
N
Legend
Crater Counting Area
Craters
Crater Counting Age Estimates
Data covers North section of mapped region
4 craters, N(1)=1.2x10^0
22 craters, N(1)=6.5x10^0
32 craters, N(1)=3.3x10^0
Cumulative Crater Frequency (km^-2)
Diameter (km)
678 +100 -100 Ma
1.35 +0.26 -0.26 Ga
2.49 +0.65 -0.82 Ga
PF: Mars, Ivanov (2001)
CF: Mars, Hartmann & Neukum (2001)
0
25
50 Km

Figure 11

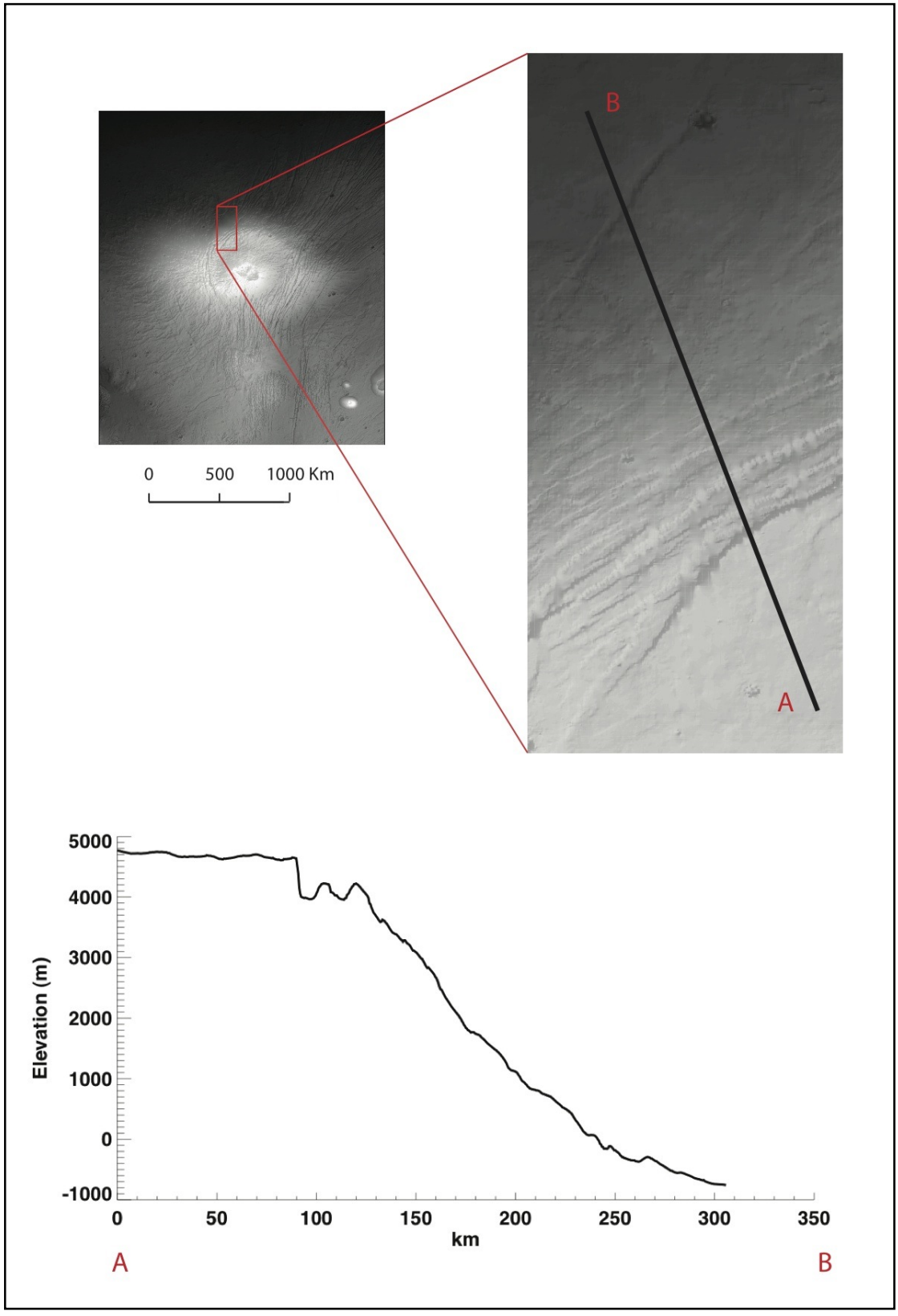
B
A
0
500
1000 Km
5000
4000
3000
2000
1000
0
-1000
Elevation (m)
0
50
100
150
200
250
300
350
km
A
B

Figure 12

REFERENCES

Acuna, M. H., J. E. P. Connerney, R. P. Lin, D. Mitchell, C. W. Carlson, J. McFadden, K. A. Anderson et al. "Global distribution of crustal magnetization discovered by the Mars Global Surveyor MAG/ER experiment." *Science* 284, no. 5415 (1999): 790-793.

Anderson, Robert C., James M. Dohm, Matthew P. Golombek, Albert FC Haldemann, Brenda J. Franklin, Kenneth L. Tanaka, Juan Lias, and Brian Peer. "Primary centers and secondary concentrations of tectonic activity through time in the western hemisphere of Mars." *Journal of Geophysical Research* 106, no. E9 (2001): 20-563.

Baker, Victor R. "Water and the Martian landscape." *Nature* 412, no. 6843 (2001): 228-236.

Baker, V.R. *et al*. Ancient oceans, ice sheets, and the hydrological cycle on Mars. *Nature* 352, 589-594 (1991)

Boynton, W. V., W. C. Feldman, S. W. Squyres, T. H. Prettyman, J. Brückner, L. G. Evans, R. C. Reedy et al. "Distribution of hydrogen in the near surface of Mars: Evidence for subsurface ice deposits." *Science* 297, no. 5578 (2002): 81-85.

Cailleau, Beatrice, Thomas R. Walter, Peter Janle, and Ernst Hauber. "Modeling volcanic deformation in a regional stress field: Implications for the formation of graben structures on Alba Patera, Mars." *Journal of geophysical research* 108, no. E12 (2003): 5141.

Carr, Michael H. "The Martian drainage system and the origin of valley networks and fretted channels." *Journal of Geophysical Research* 100.E4 (1995): 7479-7507.

Carr, Michael H. *The surface of Mars*. Vol. 6. Cambridge University Press, 2007.

Carr, Michael H., and Gary D. Clow. "Martian channels and valleys: Their characteristics, distribution, and age." *Icarus* 48.1 (1981): 91-117.

Carr, Michael H., and Gerald G. Schaber. "Martian permafrost features." *Journal of Geophysical Research* 82.28 (1977): 4039-4054.

Clancy, R. Todd, Duane O. Muhleman, and Glenn L. Berge. "Global changes in the 0–70 km thermal structure of the Mars atmosphere derived from 1975 to 1989 microwave CO spectra." *Journal of Geophysical Research* 95, no. B9 (1990): 14543-14.

Clancy, R. T., B. J. Sandor, M. J. Wolff, P. R. Christensen, M. D. Smith, J. C.

Pearl, B. J. Conrath, and R. J. Wilson. "An intercomparison of ground-based millimeter, MGS TES, and Viking atmospheric temperature measurements-Seasonal and interannual variability of temperatures and dust loading in the global Mars atmosphere." *Journal of geophysical research* 105 (2000): 9553-9571.

Connerney, J. E. P., M. H. Acuña, P. J. Wasilewski, G. Kletetschka, N. F. Ness, H. Rème, R. P. Lin, and D. L. Mitchell (2001), The global magnetic field of Mars and implications for crustal evolution, *Geophys. Res. Lett.*, *28*(21), 4015–4018, doi:10.1029/2001GL013619.

Dehant, V., Tim Van Hoolst, O. de Viron, M. Greff-Lefftz, H. Legros, and P. Defraigne. "Can a solid inner core of Mars be detected from observations of polar motion and nutation of Mars?." *Journal of geophysical research* 108, no. E12 (2003): 5127.

Marty, J. C., G. Balmino, J. Duron, P. Rosenblatt, S. Le Maistre, A. Rivoldini, V. Dehant, and Tim Van Hoolst. "Martian gravity field model and its time variations from MGS and Odyssey data." *Planetary and Space Science* 57, no. 3 (2009): 350-363.

Ferrill, David A., Danielle Y. Wyrick, Alan P. Morris, Darrell W. Sims, and Nathan M. Franklin. "Dilational fault slip and pit chain formation on Mars." *GsA Today* 14,

no. 10 (2004): 4-12.

Gulick, Virginia C., and Victor R. Baker. "Origin and evolution of valleys on Martian volcanoes." *Journal of Geophysical Research* 95.B9 (1990): 14325-14.

Hartmann, William K., and Gerhard Neukum. "Cratering chronology and the evolution of Mars." *Space Science Reviews* 96.1 (2001): 165-194.

Hess, S. L., J. A. Ryan, J. E. Tillman, R. M. Henry, and C. B. Leovy. "The annual cycle of pressure on Mars measured by Viking Landers 1 and 2." *Geophysical Research Letters* 7, no. 3 (1980): 197-200.

Hiesinger, H., J. W. Head Iii, and G. Neukum. "Young lava flows on the eastern flank of Ascraeus Mons: Rheological properties derived from High Resolution Stereo Camera (HRSC) images and Mars Orbiter Laser Altimeter (MOLA) data." *Journal of geophysical research* 112, no. E5 (2007): E05011.

Hynek, Brian M., Michael Beach, and Monica RT Hoke. "Updated global map of Martian valley networks and implications for climate and hydrologic processes." *Journal of Geophysical Research* 115.E9 (2010): E09008.

Ivanov, Boris A. "Mars/Moon cratering rate ratio estimates." *Space Science Reviews* 96.1 (2001): 87-104.

Kneissl, T., S. van Gasselt, and G. Neukum. "Map-projection-independent crater size-frequency determination in GIS environments—New software tool for ArcGIS." *Planetary and Space Science* 59.11 (2011): 1243-1254.

Leighton, Robert B., and Bruce C. Murray. "Behavior of carbon dioxide and other volatiles on Mars." *Science* 153.3732 (1966): 136-144.

Michael, G. G., et al. "Planetary surface dating from crater size-frequency distribution measurements: Spatial randomness and clustering." *Icarus* (2011).

Ivanov, Mikhail A., and James W. Head. "Alba Patera, Mars: Topography, structure, and evolution of a unique late Hesperian–early Amazonian shield volcano." *Journal of geophysical research* 111, no. E9 (2006): E09003.

McCauley, John F., M. H. Carr, J. A. Cutts, W. K. Hartmann, Harold Masursky, D. J. Milton, R. P. Sharp, and D. E. Wilhelms. "Preliminary Mariner 9 report on the geology of Mars." *Icarus* 17, no. 2 (1972): 289-327.

McSween, Harry Y., G. Jeffrey Taylor, and Michael B. Wyatt. "Elemental composition of the Martian crust." *Science* 324, no. 5928 (2009): 736-739.

Mezger, Klaus, Vinciane Debaille, and Thorsten Kleine. "Core Formation and Mantle Differentiation on Mars." *Space Science Reviews* (2012): 1-22.

Michael, G. G., and G. Neukum. "Planetary surface dating from crater size–frequency distribution measurements: Partial resurfacing events and statistical age uncertainty." *Earth and Planetary Science Letters* 294.3 (2010): 223-229.

Mouginis-Mark, P. J., Lionel Wilson, and James R. Zimbelman. "Polygenic eruptions on Alba Patera, Mars." *Bulletin of volcanology* 50.6 (1988): 361-379.

Murchie, S., R. Arvidson, P. Bedini, K. Beisser, J. P. Bibring, J. Bishop, J. Boldt et al. "Compact reconnaissance imaging spectrometer for Mars (CRISM) on Mars reconnaissance orbiter (MRO)." *J. Geophys. Res* 112, no. E05S03 (2007).

Murray, Bruce C., Laurence A. Soderblom, Robert P. Sharp, and James A. Cutts. "The surface of Mars 1. Cratered terrains." *Journal of Geophysical Research* 76, no. 2 (1971): 313-330.

Neukum, G.:1983, Meteoritenbombardement und Datierung planetarer Oberflächen, Habilitation
Dissertation for Faculty Membership, Ludwig-Maximilians Univ. Mü nchen, Munich, Germany,
186 pp.

Neukum, Gerhard, and Konrad Hiller. "Martian ages." *Journal of Geophysical Research* 86, no. 15 (1981): 3097-3121.

Neukum, G., and Wise, D.U.:1976, ‘Mars - A Standard Crater Curve and Possible new Time Scale’,
Science 194, 1381–1387.

Paige, David A. "The thermal stability of near-surface ground ice on Mars." *Nature* 356.6364 (1992): 43-45.

Pieri, David C. "Martian valleys- Morphology, distribution, age, and origin." *Science* 210.4472 (1980): 895-897.

Raitala, Jouko. "Superposed ridges of the Hesperia Planum area on Mars." *Earth, Moon, and Planets* 40.1 (1988): 71-99.

Roberts, James H., Robert J. Lillis, and Michael Manga. "Giant impacts on early Mars and the cessation of the Martian dynamo." *J. Geophys. Res* 114 (2009): E04009.

Scott, Evelyn D., and Lionel Wilson. "Plinian eruptions and passive collapse events as mechanisms of formation for Martian pit chain craters." *Journal of geophysical research* 107.E4 (2002): 5020.

Smith, Michael D. "Interannual variability in TES atmospheric observations of mars during 1999–2003." Icarus 167, no. 1 (2004): 148-165.

Stevenson, David J. "Mars' core and magnetism." *Nature* 412, no. 6843 (2001): 214-219.

Squyres, Steven W., and Michael H. Carr. "Geomorphic evidence for the distribution of ground ice on Mars." *Science* 231, no. 4735 (1986): 249-252.

Tanaka, Kenneth L. "The stratigraphy of Mars." In *Lunar and Planetary Science Conference Proceedings*, vol. 17, p. 139. 1986.

Tanaka, K. L. "Tectonic history of the Alba Patera-Ceraunius Fossae region of Mars." In *Lunar and Planetary Science Conference Proceedings*, vol. 20, pp. 515-523. 1990.

Torson, J. M., and K. J. Becker. "ISIS- A software architecture for processing planetary images." *Lunar and planetary science XXVIII* (1997): 1997.

Wilson, Lionel, and James W. Head III. "Mars: Review and analysis of volcanic eruption theory and relationships to observed landforms." *Reviews of Geophysics* 32, no. 3 (1994): 221-263.

Wyatt, Michael B., Harry Y. McSween, Kenneth L. Tanaka, and James W. Head. "Global geologic context for rock types and surface alteration on Mars." *Geology*

32, no. 8 (2004): 645-648.

Ferrill, David A., Danielle Y. Wyrick, Alan P. Morris, Darrell W. Sims, and Nathan M. Franklin. "Dilational fault slip and pit chain formation on Mars." *GsA Today* 14, no. 10 (2004): 4-12.

Vaucher, J., D. Baratoux, N. Mangold, P. Pinet, K. Kurita, and M. Grégoire. "The volcanic history of central Elysium Planitia: Implications for martian magmatism." *Icarus* 204, no. 2 (2009): 418-442.

Werner, Stephanie C. "The global martian volcanic evolutionary history." *Icarus* 201, no. 1 (2009): 44-68.

Yin, An. "An episodic slab-rollback model for the origin of the Tharsis rise on Mars: Implications for initiation of local plate subduction and final unification of a kinematically linked global plate-tectonic network on Earth." *Lithosphere* (2012).

Zuber, Maria T., Sean C. Solomon, Roger J. Phillips, David E. Smith, G. Leonard Tyler, Oded Aharonson, Georges Balmino et al. "Internal structure and early thermal evolution of Mars from Mars Global Surveyor topography and gravity." *Science* 287, no. 5459 (2000): 1788-1793.

Zurek, Richard W., Jeffrey R. Barnes, Robert M. Haberle, James B. Pollack,

James E. Tillman, and Conway B. Leovy. "Dynamics of the atmosphere of Mars." *Mars* 1 (1992): 835-933.